

# Approximating nonlinear functions with latent boundaries in low-rank excitatory-inhibitory spiking networks

William F. Podlaski\* & Christian K. Machens\*

Champalimaud Neuroscience Programme, Champalimaud Foundation, Lisbon, Portugal

July 19, 2023

## Abstract

Deep feedforward and recurrent rate-based neural networks have become successful functional models of the brain, but they neglect obvious biological details such as spikes and Dale’s law. Here we argue that these details are crucial in order to understand how real neural circuits operate. Towards this aim, we put forth a new framework for spike-based computation in low-rank excitatory-inhibitory spiking networks. By considering populations with rank-1 connectivity, we cast each neuron’s spiking threshold as a boundary in a low-dimensional input-output space. We then show how the combined thresholds of a population of inhibitory neurons form a stable boundary in this space, and those of a population of excitatory neurons form an unstable boundary. Combining the two boundaries results in a rank-2 excitatory-inhibitory (EI) network with inhibition-stabilized dynamics at the intersection of the two boundaries. The computation of the resulting networks can be understood as the difference of two convex functions, and is thereby capable of approximating arbitrary non-linear input-output mappings. We demonstrate several properties of these networks, including noise suppression and amplification, irregular activity and synaptic balance, as well as how they relate to rate network dynamics in the limit that the boundary becomes soft. Finally, while our work focuses on small networks (5-50 neurons), we discuss potential avenues for scaling up to much larger networks. Overall, our work proposes a new perspective on spiking networks that may serve as a starting point for a mechanistic understanding of biological spike-based computation.

---

\*Correspondence should be addressed to: [william.podlaski@research.fchampalimaud.org](mailto:william.podlaski@research.fchampalimaud.org); [christian.machens@neuro.fchampalimaud.org](mailto:christian.machens@neuro.fchampalimaud.org)

# Contents

<b>1</b>	<b>Introduction</b>	<b>3</b>
<b>2</b>	<b>Spiking thresholds form convex boundaries in latent space</b>	<b>6</b>
2.1	Rank-1 connectivity generates a latent variable . . . . .	6
2.2	Inhibitory neurons form stable, attracting boundaries . . . . .	8
2.3	The boundary determines the input-output mapping . . . . .	10
2.4	Excitatory neurons form unstable, repellent boundaries . . . . .	11
2.5	The inhibitory boundary can stabilize the excitatory boundary . . . . .	13
2.6	The rank-2 EI network can approximate arbitrary, non-linear input-output functions . . . . .	18
<b>3</b>	<b>Noise-controlling versus noise-amplifying networks</b>	<b>20</b>
3.1	Noise makes boundaries jitter . . . . .	20
3.2	A jittery boundary causes irregular spiking . . . . .	21
3.3	Irregular firing amplifies noise in the decoder nullspace . . . . .	22
3.4	The rank-2 EI network is inhibition-stabilized and balanced . . . . .	24
3.5	Cross-connections can suppress or amplify noise, and stability requires some level of noise control . . . . .	24
<b>4</b>	<b>Slow synapses, softer boundaries, and rate networks</b>	<b>26</b>
4.1	Slower synapses generate a finite boundary . . . . .	27
4.2	Noise causes a soft boundary . . . . .	29
4.3	The latent variables of spiking and rate networks are equivalent . . . . .	31
4.4	The EI boundaries become nullclines in the firing-rate limit . . . . .	32
4.5	Synaptic time scales impact the accuracy of the output . . . . .	34
4.6	The spike-rate equivalence requires a latent boundary . . . . .	35
<b>5</b>	<b>Discussion</b>	<b>35</b>
<b>6</b>	<b>Appendix</b>	<b>47</b>
6.1	Network parameters in the single rank-1 population . . . . .	47
6.2	Network parameters in the rank-2 EI network . . . . .	48
6.3	Function approximation in the rank-2 EI network . . . . .	48
6.4	Synaptic dynamics . . . . .	49

# 1 Introduction

The neural circuits of the brain are unbelievably complex. Yet when it comes to studying how they compute, we often resort to highly simplified network models composed of neurons with graded activation functions, i.e., rate neurons. The resulting rate networks have become the standard models of feedforward sensory processing (Yamins and DiCarlo, 2016; Lindsay, 2021) and recurrent task dynamics (Sussillo, 2014; Barak, 2017) and capture many aspects of neural circuits surprisingly well.

Of course, a mechanistic understanding of biological computation must eventually bridge back to the details of real circuits (Bernáez Timón et al., 2022). However, this task has proven surprisingly hard. Indeed, the more biologically detailed a network model is, the more difficult it tends to be to constrain and interpret (Eliasmith and Trujillo, 2014; Almog and Korngreen, 2016). We argue here that a fundamental part of this problem lies in two computational concepts of rate networks that are mismatched with biology.

The first concept is that of the ‘feature detector’ (Martin, 1994), and pertains to the difference between rate-based and spike-based coding. In a nutshell, rate neurons operate in a regime of depolarized inputs, i.e., they are activated far beyond threshold whenever the neuron’s input pattern matches its pattern of synaptic weights. In the spiking domain, unless a large amount of external noise is added, a direct translation of this idea leads to regular spike trains (Eliasmith and Anderson (2003); Fig. 1a-c). While this may be an accurate description of some biological neurons (e.g., those at the sensory periphery), cortical neurons often fire spikes irregularly (Softky and Koch, 1993). The cause of this irregularity is that such neurons operate in a fluctuation-driven regime, in which excitatory and inhibitory input currents balance each other on average (Van Vreeswijk and Sompolinsky, 1996; Shadlen and Newsome, 1998; Haider et al., 2006), and not in a strongly-depolarized regime (Fig. 1d-f). However, despite much progress (see Discussion for more details), a general theory of computation in such a regime has remained elusive. Furthermore, it has remained unclear how to perform interesting computations in smaller networks with only tens of neurons.

The second mismatched concept of rate networks concerns function approximation and its relationship to Dale’s law, i.e, the common biologically-observed distinction between excitatory and inhibitory neurons (Eccles, 1976). The flexibility of rate networks relies upon the ability of each unit to linearly combine inputs in order to represent arbitrary input-output transformations on the network level (Fig. 1c). To be most effective, the neurons’ output rates must be combined with both positive and negative weights, resulting in mixed-sign connectivity on the level of individual neurons, and thus violating Dale’s law. That said, several studies have successfully incorporated Dale’s law (e.g., Parisien et al. (2008); Song et al. (2016); Miconi (2017); Ingrosso and Abbott (2019); Shao and Ostojic (2023)), and some have even suggested potential benefits to learning and robustness (Haber and Schneidman, 2022). However, these studies have primarily taken a ‘bottom-up’ approach, incorporating Dale’s law for bio-

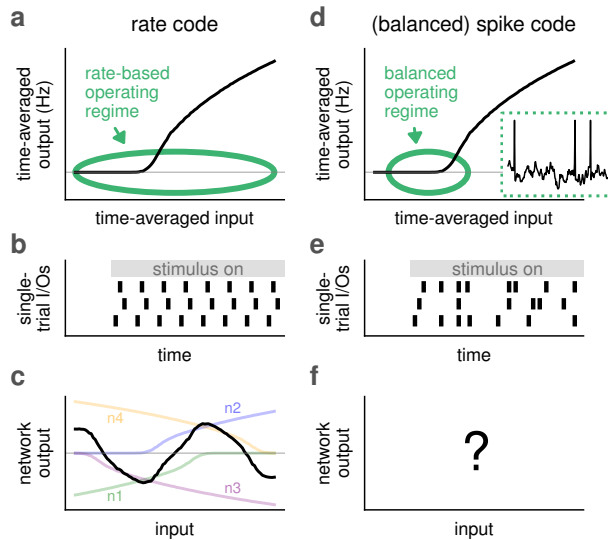


Figure 1: The operating regimes and sign constraints of rate (**a-c**) and balanced spike (**d-f**) codes are fundamentally different. **a**: A rate-coding perspective utilizes the time-averaged frequency-input (f-I) curve as a basis (shown in black for a leaky integrate-and-fire (LIF) neuron receiving noisy input); such neurons may be activated far above or below threshold (green ellipse). **b**: In the absence of additional noise, rate-coding neurons should fire regularly (3 trials shown) with a rate according to the f-I curve. **c**: Function approximation through linear-nonlinear mappings may be achieved in rate-based spiking networks (e.g., Eliasmith and Anderson (2003)); here, the black output curve is composed of the weighted sum of the four spiking neuron f-I curves (n1, green; n2, blue; n3, purple; n4, orange), with each neuron having a positive or negative output weight. **d**: A balanced-input perspective of a spiking neuron suggests a more localized operating regime with mean input below or at the neuron’s threshold (green ellipse), and thus does not follow the f-I curve (black); this balance is due to the presence of separate excitatory and inhibitory inputs (Dale’s law). **e**: This regime explains the irregular firing and trial-to-trial variability seen in cortex. **f**: It is less well-understood how such a balanced, Daleian regime may explain biological computation.

logical plausibility rather than for any computational necessity. It also remains to be seen how such sign constraints scale, as adding them to larger-scale machine learning benchmarks typically hinders (or at best matches) performance (Cornford et al., 2020; Li et al., 2023).

Neither of these mismatches is new and both have puzzled the field for a while. One common line of reasoning suggests that irregular firing and Dale’s law are two among many manifestations of biological constraints on computation. From this view, one could justify the use of abstract rate networks as idealized

versions of a constrained, noisy biological implementation. However, it is also possible that these mismatches reflect something fundamentally different about biological computation. Taking the latter perspective, here we offer a fresh approach to these puzzles.

Our study is based on a combination of two recent developments: low-rank connectivity and spike-threshold geometry. Networks with low-rank connectivities generate low-dimensional dynamics in a latent activity space (Seung, 1996; Eliasmith and Anderson, 2003; Landau and Sompolinsky, 2018; Mastrogiuseppe and Ostojic, 2018). They thereby allow the activity of individual neurons to be linked to the modes or patterns of population activities often observed in real neural circuits (Shenoy et al., 2013; Gallego et al., 2017; Saxena and Cunningham, 2019; Keemink and Machens, 2019; Jazayeri and Ostojic, 2021; Chung and Abbott, 2021; Langdon et al., 2023). Such insights can also be translated into spiking network models (Eliasmith and Anderson, 2003; Cimesa et al., 2022; DePasquale et al., 2023).

However, low-rank connectivity alone does not guarantee spike-based computation in the balanced operating regime (e.g., Eliasmith and Anderson (2003)). To achieve this, we take inspiration from spike-coding networks (SCNs) (Boerlin et al., 2013), whose function can be geometrically understood by visualizing spike-threshold boundaries in a space of latent population modes (Calaim et al., 2022). Importantly, this perspective places the boundary between sub- and supra-threshold voltages at the center of computation, leading to a fundamentally different operating regime from rate networks (Fig. 1a,d). Such networks have been shown to exhibit irregular activity, and have several other desirable biological properties like robustness and energy efficiency (Denève and Machens, 2016; Barrett et al., 2016). Based on a geometric reframing (Calaim et al., 2022; Mancoo et al., 2020), we generalize these networks here, removing several previous limitations of SCNs, while retaining their desirable properties.

We first show that a population of spiking neurons with rank-1 connectivity induces a latent variable readout and a spiking boundary in input-output space. We distinguish excitatory (E) and inhibitory (I) boundaries in this space, and show that a combined rank-2 EI network is a universal function approximator of static input-output transformations. Importantly, as we demonstrate, flexible function approximation can already be achieved in small networks, and can be theoretically understood without invoking large-network-size limits (e.g., mean field). Next, we illustrate a fundamental link between noise suppression and irregular firing, and demonstrate how mistuned connectivity between the two populations in the rank-2 EI network can lead to amplification of noise. We then consider effects of slower synaptic dynamics and transition delays on coding performance, and finally, we show that the respective low-rank spiking networks can be approximated by equivalent low-rank *rate* networks.

While we limit ourselves here to static function approximation in rank-1 populations with few neurons, in the Discussion we touch upon the implications for scaling up this framework to higher-rank networks with richer dynamical motifs, thereby providing a promising path to understand the dynamics of spiking networks in biologically-realistic regimes.

## 2 Spiking thresholds form convex boundaries in latent space

For simplicity, we will focus on networks with rank-one populations, and use them to develop the central concepts of this paper: latent variables and convex boundaries. Following an introduction of the general rank-1 case, we will distinguish inhibitory (I) and excitatory (E) populations. Then, we will combine the two populations into a rank-two EI network, and illustrate the resultant dynamics and input-output transformations.

### 2.1 Rank-1 connectivity generates a latent variable

Let us consider a network of  $N$  recurrently connected spiking neurons. We denote each neuron’s membrane potential by  $V_i$  and assume that the neuron fires a spike when it reaches a threshold,  $T$ . Each neuron’s membrane potential will be described as a leaky integrate-and-fire neuron,

$$\tau \dot{V}_i(t) = -V_i(t) + F_i c(t) + \sum_{j=1}^N W_{ij} s_j(t) + b_i. \quad (1)$$

Here the first term on the right-hand-side describes a leak current, the second term a feedforward input,  $c(t)$ , weighted by synaptic feedforward weights,  $F_i$ , the third term the recurrent spike trains,  $s_j(t)$ , of presynaptic neurons, each weighted by recurrent synaptic weights,  $W_{ij}$  (without sign constraints for now), and the last term is a constant background input. The constant background simply shifts the effective threshold of the neuron, and can therefore be modeled equivalently by setting  $b_i = 0$  and assuming an effective neural threshold  $T_i$ . For simplicity, we also set the neuron’s membrane time constant  $\tau = 1$ , so that the unit of time corresponds to  $\tau$  (set to 10 ms for all simulations).

We model each neuron’s spike trains as a series of delta functions, such that  $s_i(t) = \sum_f \delta(t - t_i^f)$ , where  $t_i^f$  is the time of the  $f$ -th spike of the  $i$ -th neuron. Importantly, for now we assume instantaneous communication between neurons without temporal synaptic dynamics or delays (this will be relaxed in Section 4; see Appendix). We furthermore assume that the diagonal of the weight matrix,  $W_{ii}$ , includes the voltage reset after a spike, thereby setting the reset voltage to

$$V_{i,\text{reset}} = T_i - W_{ii}. \quad (2)$$

For our exposition, we will mostly rely on the integrated version of these equations (Gerstner et al., 2014; Calaim et al., 2022). Let us first define the filtered input,  $x(t)$ , and the filtered spike trains,  $r_i(t)$ , as

$$\dot{x}(t) = -x(t) + c(t) \quad (3)$$

$$\dot{r}_i(t) = -r_i(t) + s_i(t). \quad (4)$$

These equations express a filtering or convolution of the input or spike trains, respectively, with a one-sided exponential kernel,  $h(t) = H(t) \exp(-t)$ , where

$H(t)$  is the Heaviside function (i.e.,  $H(t) = 1$  if  $t \geq 0$ , and  $H(t) = 0$  otherwise). Accordingly, we can think of  $r_i(t)$  as a simple model of a neuron’s postsynaptic potential, or as a (single-trial) estimate of a neuron’s firing rate.

With these definitions, we can integrate Eq. (1) to obtain

$$V_i = F_i x + \sum_{j=1}^N W_{ij} r_j, \quad (5)$$

where we have dropped the time index for brevity. By taking the derivative of this equation, and inserting the equations for the filtered inputs and spike trains, Eqs. (3) and (4), one retrieves Eq. (1). A key assumption for this section will be that the weight matrix has rank one, so that we can write

$$W_{ij} = E_i D_j. \quad (6)$$

where we will call the scalars  $E_i$  the encoding weights and  $D_j$  the decoding weights. With this definition, the integrated voltage equation, Eq. (5), becomes

$$V_i = F_i x + \sum_{j=1}^N E_i D_j r_j \quad (7)$$

$$= F_i x + E_i \left( \sum_{j=1}^N D_j r_j \right). \quad (8)$$

The term inside the brackets is simply a linear combination of the filtered spike trains, independent of index  $i$ . We will denote it as

$$y = \sum_{j=1}^N D_j r_j, \quad (9)$$

so that the voltage becomes

$$V_i = F_i x + E_i y. \quad (10)$$

Importantly, the variable  $y$  fully controls the dynamics of the network, in that knowledge of  $y$  (together with the input  $x$ ) is sufficient to compute the voltages, and consequently the spike trains. We will refer to  $y$  as the readout, the output, or the *latent variable* of the network.

We emphasize that linear, weighted sums of filtered spike trains are a common motif not only in the study of neural networks, but also in the analysis of population recordings (Fusi et al., 2016; Saxena and Cunningham, 2019; Keemink and Machens, 2019; Vyas et al., 2020; Jazayeri and Ostojic, 2021). Indeed, such ‘linear readouts’ are a standard means of extracting information from neural recordings, either through explicit linear decoding (Dayan and Abbott, 2005) or through the use of linear dimensionality reduction methods such as principal components analysis or factor analysis (Cunningham and Yu, 2014). Consequently, we can also view  $y$  as a component or mode of population activity.

## 2.2 Inhibitory neurons form stable, attracting boundaries

So far we have not put any sign constraints on the connectivity. Now considering a population of inhibitory neurons with negative weights, we impose

$$W_{ij} = E_i D_j \leq 0 \quad \forall i, j, \quad (11)$$

by requiring

$$E_i \geq 0 \quad \forall i, \quad (12)$$

$$D_j \leq 0 \quad \forall j. \quad (13)$$

With this sign convention, the negative sign is associated to the decoding weights, and from Eq. (9), the latent variable or readout will also be constrained to be negative,  $y \leq 0$ . The voltage equation, Eq. (10), remains unchanged, but the positive encoding weights  $E_i$  and negative latent variable,  $y$ , ensure that each neuron receives negative feedback from the inhibitory population.

Our first goal will be to understand the dynamics of the integrate-and-fire network in the joint space of inputs and readouts. Using Eqs. (4) and (9), we can compute the derivative of the readout,

$$\dot{y} = -y + \sum_{j=1}^N D_j s_j, \quad (14)$$

revealing the dynamics to be a weighted, leaky integration of the network’s spike trains. These dynamics therefore fall into two regimes:

$$\begin{aligned} \dot{y} &= -y \\ y &\leftarrow y + D_i \quad \text{if} \quad V_i = F_i x + E_i y \geq T_i. \end{aligned} \quad (15)$$

Either the readout is leaking towards zero (top equation) or it is changing abruptly due to spikes (bottom equation).

To gain more intuition for these separate regimes, let us start with a single neuron. For this neuron, the equation  $V_1 = F_1 x + E_1 y = T_1$  defines a line in  $(x, y)$ -space, i.e., in the space of inputs and outputs (Fig. 2a, solid blue). On one side of the line, the neuron is subthreshold, and on the other side, it is suprathreshold. The output  $y$  always leaks towards zero in the absence of firing. Once the neuron’s threshold is hit, it fires, and the readout bounces down according to the size of the neuron’s decoder weight, to  $y \leftarrow y + D_i$ . The neuron’s inhibitory self-connection acts as a reset, moving the voltage from threshold ( $V_1 = T_1$ ) down to a hyperpolarized value (Fig. 2a, dotted blue line).

Now considering a network of several neurons, each threshold will trace a different line in the input-output space (Fig. 2b) and together they will form a single boundary (Fig. 2b, gray dashed line; Fig. 2c, solid blue line). We will use ‘subthreshold’ to denote the region where *all* neurons’ voltages are below threshold and ‘suprathreshold’ to denote the region where *at least one* neuron is above threshold. Since  $E_i \geq 0$ , the subthreshold region lies below each



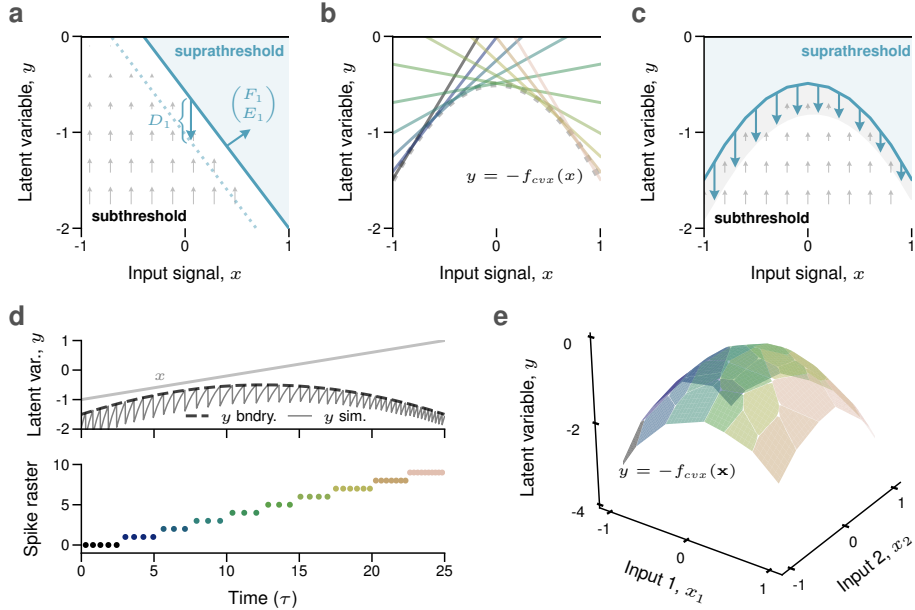


Figure 2: A rank-1 inhibitory population forms a stable, attracting boundary. **a:** A single inhibitory neuron’s voltage (Eq. (10)) is visualized in input-output space; the spiking threshold ( $V_1 = T_1$ ; solid blue line) divides the space into sub- and supra-threshold sets, with leak dynamics (gray arrows) and spiking at the boundary, incrementing  $y \rightarrow y + D_1$ , and resetting the voltage to  $V_1 = T_1 - W_{11}$  (dotted blue line). **b:** The thresholds of multiple ( $N = 10$ ) neurons were tuned to delineate a concave (or negative convex) boundary in input-output space,  $y = -f_{cvx}(x) = -x^2 - \frac{1}{2}$ . **c:** The boundary divides the input-output space into a convex subthreshold set (with *all* voltages below threshold), and a suprathreshold set (with *at least one* voltage above threshold), forming a stable input-output relationship. Output precision is defined as the distance between the neural thresholds and the resets after a spike, which can be different for each neuron (gray shading; see Eq. (18)). **d:** Latent variable output (top) and spike raster (bottom) of a simulation of the spiking network from panel **c** for a time-varying input from  $x = -1$  to  $1$  (gray line); the simulation output follows the true boundary, and each input value is coded by a single neuron. **e:** A negative convex surface boundary for a two-dimensional input, made up of 36 neurons (colored segments) which tile the space.

neuron’s threshold line. Just as in the single-neuron case, the latent variable,  $y$ , leaks towards zero until it reaches the boundary, where a neuron will fire a spike, causing  $y$  to jump back into the subthreshold region, and the dynamics continue. Note that this jump into the subthreshold region pushes  $y$  away from all threshold boundaries, and therefore corresponds to recurrent inhibition between all neurons. Since each part of the boundary is covered by a single

neuron, only one neuron will fire spikes for each value of the input  $x$  (Fig. 2d).

We emphasize that *any* integrate-and-fire network following Eq. (1) and assuming the sign and rank-constraints,  $W_{ij} = E_i D_j \leq 0$ , will form a stable spike-threshold boundary. However, a rank-1 population with randomly-distributed parameters,  $(F_i, E_i, T_i)$ , will, more often than not, yield a boundary composed of only a subset of neurons (not shown). In other words, some neurons' boundaries will be well within the supra-threshold set, and so will never fire any spikes. Furthermore, a random boundary may also cross the  $x$ -axis ( $y = 0$ ), resulting in some input values for which no neuron is active. Since such parameter regimes include silent neurons or fully silent activity regimes, we consider them degenerate and do not consider them. Instead, the networks shown in Fig. 2b,c,e were precisely tuned so that each neuron's threshold lies along a smooth quadratic function (see Appendix for details).

### 2.3 The boundary determines the input-output mapping

The concept of a boundary in the input-output space will be central to our developments. This perspective can also be generalized to rank-1 networks with multiple inputs. Let us write  $\mathbf{x} = (x_1, x_2, \dots, x_M)$  for an  $M$ -dimensional input, in which case the voltage equation becomes

$$V_i = \mathbf{F}_i^T \mathbf{x} + E_i y \leq T_i. \quad (16)$$

This inequality still describes a linear boundary, but now in a higher-dimensional input-output space,  $(\mathbf{x}, y) \in \mathbb{R}^{M+1}$ . Multiple neurons again define different boundaries, each of which divides the input-output space into two half-spaces. To formalize the resultant population boundary, we will write

$$y = -f_{\text{cvx}}(\mathbf{x}) \quad (17)$$

where  $f_{\text{cvx}}(\mathbf{x})$  denotes a (piecewise-linear) convex function. The negative sign implies that  $y$  is actually a *concave* function of the inputs  $x$ . More broadly speaking, however, since the subthreshold region is defined by the intersection of a set of half-spaces, the central mathematical concept is that of a convex subthreshold set and its associated convex boundary (Discussion). For  $\mathbf{x} \in \mathbb{R}^2$ , we plot an example boundary in Fig. 2e.

The above function serves as an idealized description of the network's input-output relationship. More precisely, the output of the network jumps back and forth between this threshold boundary and the set of  $y$ -values that is reached after a spike (Fig. 2d). Since every input  $\mathbf{x}$  can be uniquely associated with the neuron whose boundary is exposed, we can define a 'decoder' function,  $\mathcal{D}(\mathbf{x}) \leq 0$ , which takes the value of the decoder for the neuron that becomes active for input  $x$ . Accordingly, the output takes values in the interval

$$y = [-f_{\text{cvx}}(\mathbf{x}) + \mathcal{D}(\mathbf{x}), -f_{\text{cvx}}(\mathbf{x})]. \quad (18)$$

We refer to this deviation from the "true" boundary,  $-f_{\text{cvx}}(\mathbf{x})$ , caused by discrete spiking events, as the *precision* by which the input is mapped onto the

output, as determined by the function  $\mathcal{D}(\mathbf{x})$  (compare Fig. 2c, gray shading and Fig. 2d).

In summary, we can write down the dynamics of  $y$  in two equivalent ways. First, we can think of each individual neuron as enforcing its own threshold, and we can think of the boundary as the joint action of all thresholds. Merging the two dynamical regimes, Eq. (15), into a single equation, we obtain

$$\dot{y} = -y + \sum_{i=1}^N D_i I(\mathbf{F}_i^\top \mathbf{x} + E_i y - T_i), \quad (19)$$

where the indicator function  $I(\cdot)$  denotes an infinitely high boundary, i.e.,  $I(z) = \infty$  if  $z \geq 0$  and  $I(z) = 0$  otherwise. The indicator function is commonly used in convex analysis (Rockafellar, 1997; Boyd and Vandenberghe, 2004), and can be understood similarly to the delta-function used in spiking networks, i.e., as a limiting case,  $I(z) = \lim_{\Delta t \rightarrow 0} H(z)/\Delta t$ , where  $H(z)$  is the Heaviside function, and  $\Delta t$  the integration time step.

Second, we can think of the network as forming a single (globally) stable boundary

$$\dot{y} = -y + \mathcal{D}(\mathbf{x}) I(B(\mathbf{x}, y)). \quad (20)$$

using the decoder function  $\mathcal{D}(\mathbf{x})$  and similarly defining a boundary function

$$B(\mathbf{x}, y) = y + f_{\text{cvx}}(\mathbf{x}), \quad (21)$$

where we can recover our definition of the boundary input-output function by setting  $B(\mathbf{x}, y) = 0$ . Eqs. (19) and (20) are mathematically equivalent, and both will prove useful later on.

## 2.4 Excitatory neurons form unstable, repellent boundaries

Next, we consider a network of  $N$  recurrently connected, excitatory neurons. Much of our exposition follows the same outline as for the inhibitory network, and we will mostly focus on highlighting the differences. Of course, the key difference is positive connectivity, compared to Eq. (11),

$$W_{ij} = E_i D_j \geq 0, \quad (22)$$

with constraints on the encoders and decoders

$$E_i \geq 0 \quad \forall i, \quad (23)$$

$$D_j \geq 0 \quad \forall j. \quad (24)$$

Given these sign conventions for the excitatory network, the latent variable or readout will be constrained to be positive,  $y \geq 0$ . The voltage equation, Eq. (10), again remains the same, but now each neuron receives positive feedback from itself and all other neurons of the excitatory population.

We note that due to the positivity constraint, even the diagonal terms of the connectivity matrix,  $W_{ii}$ , are all positive. For the inhibitory network, in contrast, the diagonal terms were negative and thereby corresponded to the self-reset current after a spike. A positive diagonal term here means that the neuron will self-excite, and thereby immediately fire more spikes. While the absence of a reset term may seem unnatural, it provides a useful entry point for studying low-rank, all-excitatory networks in their idealized form. (In practice, a self-reset can be introduced, which we describe below; also see Appendix).

The dynamics of a purely-excitatory network are visualized in Fig. 3. Once more, each neuron divides the input-output space into two halves, and the boundary of these half spaces is given by equating the voltage equation (Eq. (10)) with the threshold, i.e.,  $V_i = T_i$  (Fig. 3a). The sub- and suprathreshold regions are similarly defined as in the all-inhibitory network and are shown for a single neuron or several neurons in Fig. 3a,b. The output  $y$  is now positive, and still leaks towards zero in the subthreshold region, but now this leak is *away* from the boundary. If the boundary is breached, however, the respective neuron fires, which moves the latent variable further into the supra-threshold regime. This causes self-excitation of the firing neuron, but also potentially crossing the thresholds of other neurons. (Strictly speaking, the firing of multiple neurons is mathematically ill-defined. For now, we will be pragmatic, discretize time, and assume that only one neuron can fire per time step (see Appendix). In Section 4, we will relax this assumption.) In consequence, the dynamics beyond the boundary self-reinforces the growth of the output and becomes highly explosive (Fig. 3c). To illustrate the unstable dynamics on either side of the boundary, the boundary function in Fig. 3b,c was chosen such that  $y = 0$  is contained within the subthreshold set for the displayed values of  $x$ , meaning that in the absence of previous spiking, the network will remain silent. This choice is primarily illustrative, and we will return to the spontaneously-active case in the next section after re-introducing inhibition.

Just as in the inhibitory network, the set of subthreshold readouts is a convex set, and the boundary is a concave function of the input within a given range (see Fig. 3). The same reasoning holds when the input  $\mathbf{x}$  becomes multi-dimensional. We can therefore characterize the unstable boundary through a concave function,

$$y = -f_{\text{cvx}}(\mathbf{x}), \quad (25)$$

defined on the set of inputs,  $\mathbf{x}$ , for which  $y \geq 0$ . Since this boundary is unstable, it does not per se describe the input-output mapping of an all-excitatory network. Indeed, the input-output mapping of the network will be determined by the mechanism(s) that stabilize the explosion (see below). Finally, we can summarize the dynamics of the excitatory network using Eqs. (19) and (20), with the key difference that  $D_i$  or  $\mathcal{D}(\mathbf{x})$  are now positive, which inverts the dynamics around the boundary.

Given that the excitatory population is unstable, some other mechanisms need to kick in to stabilize the dynamics. One stabilizing factor is the leak of each neuron, which eventually could counter the explosion of activity. A second

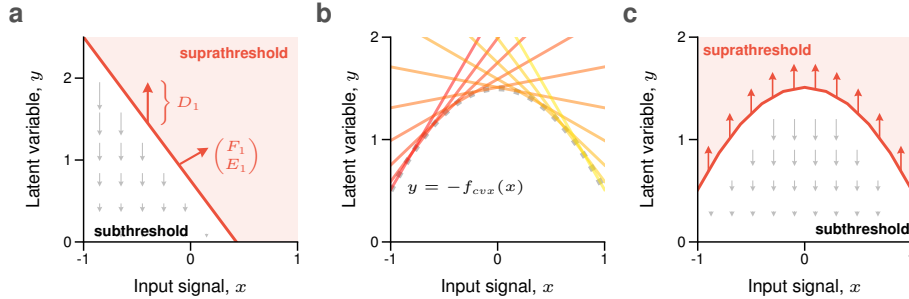


Figure 3: A rank-1 excitatory population forms an unstable, repellent boundary. **a**: Input-output space for a single excitatory neuron (compare with Fig. 2a). Note that a spike moves the latent variable further into the supra-threshold set. **b**: The thresholds of multiple ( $N = 10$ ) excitatory neurons were tuned to delineate a concave (or negative convex) boundary in input-output space,  $y = -f_{cvx}(x) = -x^2 + \frac{3}{2}$ . **c**: The boundary forms a convex subthreshold set (where *all* voltages are below threshold), analogous to the inhibitory population (Fig. 1). Unlike the inhibitory population, however, the boundary itself is now unstable — it either leaks to zero or explodes.

approach would be to give each excitatory neuron a self reset and/or refractory period after firing a spike. This can be formalized by adding a diagonal component  $\mu$  to the connectivity matrix such that

$$W_{ii} = E_i D_i - \mu, \quad (26)$$

which serves as a “soft” refractory period (Calaim et al., 2022). Though technically this breaks the assumed low-rank connectivity structure, it will prove useful, and we will return to it in Section 3. Finally, a third possibility is to stabilize the network activity with inhibition, which we will do next.

Before moving on, we make one additional comment about Dale’s law here. The concepts of stable and unstable spike-threshold boundaries form the main computational components of our framework. Intriguingly, sign-constrained inhibitory and excitatory populations are sufficient to generate such well-behaved boundaries, and we will see below how the combination of the two leads to a unique computational regime. We note that while a stable boundary can be generated without adhering to Dale’s law, as is known from previous work on spike-coding networks (Calaim et al., 2022), the stability is only local and can rapidly explode upon certain perturbations (see Discussion).

## 2.5 The inhibitory boundary can stabilize the excitatory boundary

We now study networks of coupled excitatory (E) and inhibitory (I) neurons. In order to do so, we will first go back to differential equations. Assuming that there are  $N^I$  inhibitory and  $N^E$  excitatory neurons, we again use leaky

integrate-and-fire neurons to describe the membrane potentials of the two populations,

$$\dot{V}_i^I = -V_i^I + F_i^I c(t) + \sum_{j=1}^{N^E} W_{ij}^{IE} s_j^E(t) + \sum_{j=1}^{N^I} W_{ij}^{II} s_j^I(t) \quad (27)$$

$$\dot{V}_i^E = -V_i^E + F_i^E c(t) + \sum_{j=1}^{N^E} W_{ij}^{EE} s_j^E(t) + \sum_{j=1}^{N^I} W_{ij}^{EI} s_j^I(t). \quad (28)$$

Besides the self-connections within the subnetworks,  $W^{EE}$  and  $W^{II}$ , we also introduce cross-connections between the two networks, designated by the matrices  $W^{EI}$  and  $W^{IE}$ . The thresholds of the two populations are given by  $T_i^I$  and  $T_i^E$ , and as before, may incorporate possible background inputs.

Just as before, we assume that the self-connection matrices are rank-1. We will furthermore assume that the cross-connection matrices are likewise rank-1, while sharing the same decoders. Specifically, we set (for all  $i, j$ )

$$W_{ij}^{II} = E_i^{II} D_j^I \leq 0 \quad (29)$$

$$W_{ij}^{IE} = E_i^{IE} D_j^E \geq 0 \quad (30)$$

$$W_{ij}^{EI} = E_i^{EI} D_j^I \leq 0 \quad (31)$$

$$W_{ij}^{EE} = E_i^{EE} D_j^E \geq 0, \quad (32)$$

resulting in a rank-2 excitatory-inhibitory (EI) network. These settings are not fully general, as the cross-connection matrices could, in principle, have their own set of decoders. We will defer the analysis of the general case to Section 3. All the encoding weights are assumed to be positive, while the decoders follow previously-specified sign constraints, i.e.,  $D_j^I \leq 0$  and  $D_j^E \geq 0$ , ensuring Dale's law.

Given the above assumptions, we define two latent variable readouts,

$$y^I = \sum_{j=1}^{N^I} D_j^I r_j^I \quad (33)$$

$$y^E = \sum_{j=1}^{N^E} D_j^E r_j^E. \quad (34)$$

which allows us to integrate the differential equations and obtain

$$V_i^I = F_i^I x + E_i^{IE} y^E + E_i^{II} y^I \leq T_i^I \quad (35)$$

$$V_i^E = F_i^E x + E_i^{EE} y^E + E_i^{EI} y^I \leq T_i^E. \quad (36)$$

We see that even in this more complicated network, each neuron can once more be interpreted as a bound in input-output space. The key difference is that we now have a rank-2 network, and the input-output space has become three-dimensional, given by  $(x, y^E, y^I) \in \mathbb{R}^3$ . As a consequence, neural thresholds

have become planes instead of lines. Furthermore, we now have two distinct sets of spike-threshold boundaries, corresponding to the two populations.

The spiking dynamics of the network can again be understood by focusing on the space of latent variables, which is now two-dimensional. Taking the derivative of the readout equations, we obtain the two-dimensional dynamics of the latent space, compare Eq. (19),

$$\dot{y}^I = -y^I + \sum_{i=1}^{N^I} D_i^I I(F_i^I x + E_i^{IE} y^E + E_i^{II} y^I - T_i^I) \quad (37)$$

$$\dot{y}^E = -y^E + \sum_{i=1}^{N^E} D_i^E I(F_i^E x + E_i^{EE} y^E + E_i^{EI} y^I - T_i^E). \quad (38)$$

We have already done all the work to understand these equations. In the first equation, for instance, we can simply understand  $y^E$  as a (time-varying) external input. As a consequence, we can treat the inhibitory population as receiving a two-dimensional input,  $(x, y^E)$  (see Fig. 2e), so that the derivations from Section 2.2 all remain the same. Similarly, the excitatory population can be treated as receiving a two-dimensional input  $(x, y^I)$ . Accordingly, the inhibitory dynamics generates a stable boundary in  $(x, y^E, y^I)$ -space, and the excitatory dynamics generates an unstable boundary in  $(x, y^E, y^I)$ -space.

Example boundaries for the inhibitory and excitatory populations are shown in Fig. 4a,b, respectively. The blue boundary describes the inhibitory population, and is a negative convex function of  $x$  and  $y^E$ , denoted  $y^I = -f_{\text{cvx}}^I(x, y^E)$ . Note that it is illustrated here as a smooth continuous surface, but in reality will be piecewise linear, made up of individual neurons' thresholds as in Fig. 2e. Since all decoders are negative, each spike of an inhibitory neuron drives the readout into the subthreshold regime, and the state space is restricted to negative values of  $y^I$  (Fig. 4a). Similarly, the excitatory population is described by the red, negative convex boundary (Fig. 4b), which is a function of  $x$  and  $y^I$ , denoted  $y^E = -f_{\text{cvx}}^E(x, y^I)$ . However, in this case each excitatory spike drives the readout into the suprathreshold regime towards positive values of  $y^E$ .

Following Eq. (20), we can also rewrite the dynamics in terms of the boundaries only,

$$\dot{y}^I = -y^I + \mathcal{D}^I(x, y^E) I(B^I(x, y^E, y^I)) \quad (39)$$

$$\dot{y}^E = -y^E + \mathcal{D}^E(x, y^I) I(B^E(x, y^E, y^I)) \quad (40)$$

where the boundary functions are given by  $B^I(x, y^E, y^I) = f_{\text{cvx}}^I(x, y^E) + y^I$  and  $B^E(x, y^E, y^I) = f_{\text{cvx}}^E(x, y^I) + y^E$ , and the boundaries are retrieved by setting them to zero. To visualize the dynamics of this joint system, we assume a constant input  $x$ , which means that the two boundary surfaces reduce to 1-d curves in  $(y^E, y^I)$ -space (shown as the blue and red lines in Fig. 4a,b, respectively for  $x = 4$ ). Both boundaries are plotted together in Fig. 4c. Here, we have chosen to plot the absolute value of the inhibitory readout,  $|y^I|$ , as it is

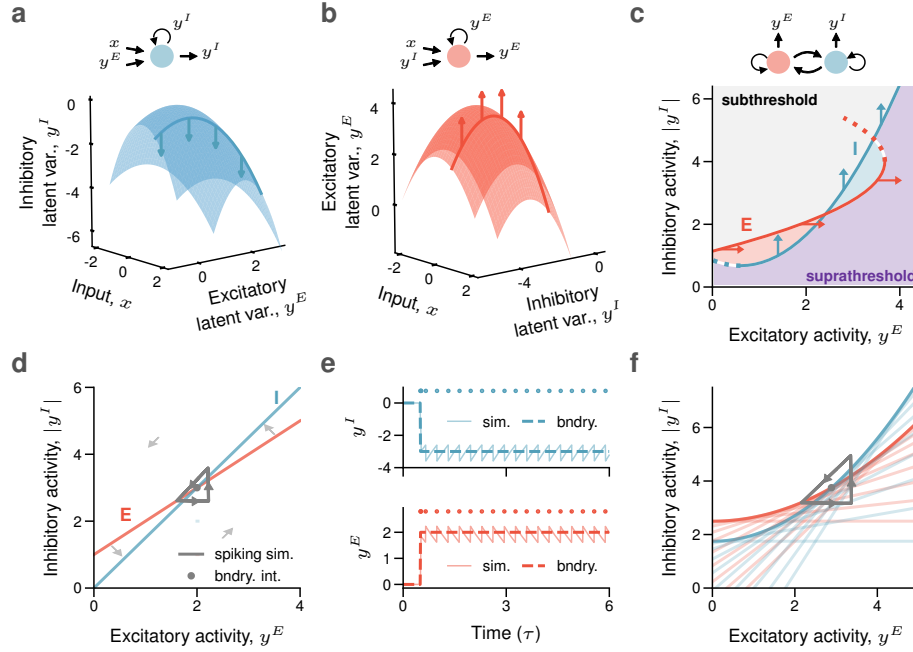


Figure 4: The inhibitory boundary can stabilize the excitatory boundary. **a**: The inhibitory population, with latent readout  $y^I$ , forms a negative convex, attracting boundary in  $(x, y^E)$  space. **b**: The excitatory population, with latent readout  $y^E$ , forms a negative convex, repellant boundary in  $(x, y^I)$  space. **c**: For fixed  $x$  (blue and red lines in panels **a** and **b**, respectively for  $x = 4$ ), the inhibitory and excitatory boundaries can be viewed in  $(y^E, y^I)$  space, and delineate four distinct regions of the state space:  $E$  and  $I$  subthreshold (gray),  $E$  suprathreshold and  $I$  subthreshold (red),  $E$  subthreshold and  $I$  suprathreshold (blue), and both  $E$  and  $I$  suprathreshold (purple). **d,e**: Single-neuron  $E$  and  $I$  boundaries with dynamics (gray in panel **d**; blue and red solid lines in **e**) around the boundary crossing (black dot in **d**; blue and red dashed lines in **e**). Dots in panel **e** show the spikes fired. **f**: Heterogeneous  $E$  and  $I$  boundaries, in which  $I$  (respectively  $E$ ) neurons form a piecewise-linear approximation to the convex boundaries. Dynamics are shown in gray, oscillating around the boundary crossing (gray dot).

comparable to the summed population activity (especially if decoders are constant,  $\mathcal{D}^I(x, y^E) = \text{const}$ ), and related to typical ways of looking at EI networks (Wilson and Cowan, 1972; Dayan and Abbott, 2005; Gerstner et al., 2014).

We see that the two boundaries intersect (Fig. 4c), and we can distinguish four regions of the state-space around this intersection. If both populations are below threshold, the population activities will simply leak toward zero (gray area in Fig. 4c). If one population is suprathreshold and the other subthreshold (red or blue areas in Fig. 4c), then the suprathreshold population activity



increases rapidly (through spiking) while the subthreshold activity decreases slowly (through the leak). If both populations are suprathreshold, both activities increase rapidly (purple areas in Fig. 4c). In order to eliminate any ambiguities in the suprathreshold regime, and to promote stability, we will prescribe that inhibitory neurons always fire before excitatory neurons when both are above threshold. This somewhat ad hoc rule implies that inhibition generally has faster dynamics than excitation, and will be relaxed later in Section 4.

The latent dynamics of the EI system in Fig. 4c will tend to gravitate around the point at which the two boundaries cross. The dynamics resemble a stable limit cycle, which, in the limit as the decoders become smaller and smaller, effectively becomes a stable fixed point for certain requirements of the two boundaries. Intuitively, we can understand the stability of the EI system by considering the slopes of the two boundaries in  $(y^E, |y^I|)$ -space (Fig. 4d). Under the rule that inhibitory neurons always fire before excitatory neurons, local stability requires the inhibitory boundary to have a steeper slope, such that it is able to push the dynamics into the subthreshold area when the readouts are above the crossing point. For instance, if the network is composed of one inhibitory neuron and one excitatory neuron (Fig. 4d), this slope condition can be succinctly expressed through the encoding weights as

$$\frac{E_1^{IE}}{E_1^{II}} > \frac{E_1^{EE}}{E_1^{EI}}, \quad (41)$$

where both neurons have been labeled with index  $i = 1$ . This inequality is analogous to the condition on the determinant in a two-dimensional linear stability analysis (Izhikevich, 2007). A more formal treatment of stability can be done after relating the spiking dynamics to those of a rate network (Section 4; (Dayan and Abbott, 2005; Izhikevich, 2007)). We also note that other stable dynamical regimes may be present in the more general case, such as networks in which the excitatory or both populations are silent. As before, we consider these to be degenerate and do not discuss them here.

To understand the stable EI dynamics produced by this picture, we simulate the two-neuron system in Fig. 4d,e. Here, we have a single excitatory and a single inhibitory neuron. When the two outputs  $y^I$  and  $y^E$  leak towards zero, both neurons experience a decrease in recurrent inhibition and recurrent excitation, resulting in an overall depolarization of both neurons. The excitatory neuron fires first, and the output  $y^E$  moves to the right. At this point, both neurons experience an excitatory postsynaptic current. The inhibitory neuron then crosses threshold and, according to our rule above, fires before the excitatory neuron can fire another spike. The inhibitory spike inhibits the excitatory neuron and moves the output  $(y^E, |y^I|)$  into the subthreshold set of both neurons. At this point, the dynamics repeat. While globally stable, the local dynamics of the limit cycle, and repeatability of the spiking pattern, not only depends on the shapes of the boundaries, but also the decoding weights (see Appendix). Principally the same pattern is observed when we consider a network with several neurons in each population (Fig. 4f). In the deterministic regime that we consider in this Section, this oscillatory pattern only encompasses the two neurons

that make up the crossing point for the given input  $x$  (and local stability can still be assessed with Eq. (41)), but the latent dynamics are reflected in all neurons' voltages (not shown).

We note that in the general case, with multiple neurons per population, the E and I boundaries can in principle cross multiple times, leading to more interesting dynamics such as bistability (not shown, but see Discussion).

## 2.6 The rank-2 EI network can approximate arbitrary, non-linear input-output functions

As shown above, provided that stability conditions are satisfied, the dynamics of the rank-2 EI network will converge towards an oscillation around the crossing point of the two boundaries. Crucially, this crossing point depends on the input  $x$ . If we add this third dimension back to the picture, we see that the crossing point between the two populations can vary if different neurons form the boundary at different values of  $x$  (Fig. 5a). It turns out that such an approach can yield a rich set of possible input-output functions. Indeed, while the above equations cannot generally be solved for  $y^I$  or  $y^E$ , we can show that each latent variable on its own can, in principle, be any function of the input  $x$ .

We assume that the inhibitory boundary has the form

$$y^I = -f_{\text{cvx}}^I(x, y^E) = -p(x) - ay^E, \quad (42)$$

where  $p(x)$  is some convex function, and  $a$  is a positive constant. Then, we assume the excitatory boundary has the form

$$y^E = f_{\text{cvx}}^E(x, y^I) = -q(x) - y^I, \quad (43)$$

where  $q(x)$  is also a convex function. We note that the stability condition, Eq. (41), requires  $a > 1$ , which ensures that the inhibitory boundary has a larger slope than the excitatory boundary. Given that the input-output function will be described by the crossing of the two boundaries, we can rewrite the excitatory latent variable as

$$y^E = -q(x) - y^I \quad (44)$$

$$= -q(x) + p(x) + ay^E. \quad (45)$$

Finally, rearranging terms and setting  $a = 2$ , we obtain

$$y^E = q(x) - p(x), \quad (46)$$

which is the difference of two convex functions. Instead solving for  $y^I$ , we get

$$y^I = p(x) - 2q(x), \quad (47)$$

which is again the difference of two convex functions. Since any function with a continuous second derivative ( $C^2$ ) can be expressed as the difference of two

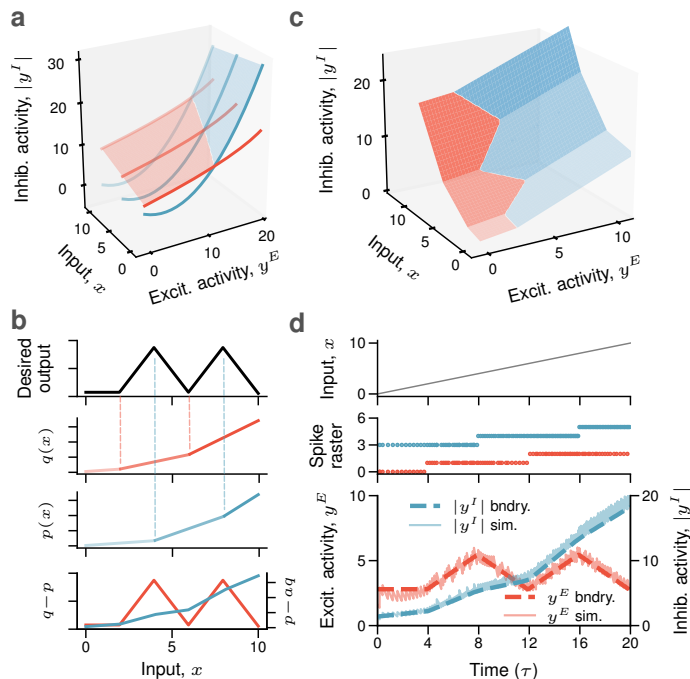


Figure 5: Universal function approximation in the rank-2 EI network. **a**: Considering the EI network dynamics as a function of the input,  $x$ , yields a network that is able to modulate the boundary crossing as a function of input. **b**: A desired saw-like output function (top) can be decomposed into the difference of two convex functions  $q(x)$  and  $p(x)$  (middle), such that the excitatory latent variable approximates the function (bottom). **c**: Visualization of a network of  $N^E = 3$  excitatory (red) and  $N^I = 3$  inhibitory (blue) neurons that approximates the saw-like function following panel **b**. **d**: Simulating the spiking network from **c** for an input  $x$  from 0 to 10 confirms that the input-output function of the network approximates the boundary crossing.

convex functions (Hartman, 1959; Horst and Thoai, 1999; Lipp and Boyd, 2016), the input-output function of the rank-2 E-I network is fully general. Accordingly, the limitations to computations imposed by the boundaries of the separate populations disappear once excitatory and inhibitory populations are coupled. Furthermore the interpretation of the input-output transformation as computing a difference of two convex function puts forth an intriguing computational hypothesis for the function of Dale’s law (see Discussion).

A toy example of function approximation is shown in Fig. 5b-d, in which a non-convex, saw-like function is approximated by the excitatory latent readout of a small network with  $N^E = 3$  and  $N^I = 3$  neurons. Such a network computation is intuitively straightforward to visualize and to construct (see Appendix). Following the notation above, we can simply design piecewise-linear convex func-

tions  $p(x)$  and  $q(x)$  such that their difference approximates (or equals, in this case) the desired function (Fig. 5b). We note that more continuous functions can be approximated with more neurons, and similar non-convex approximations can also be done with the inhibitory readout (not shown).

While the above derivation was done for a one-dimensional input  $x$ , it also holds for  $M$ -dimensional inputs, so that the rank-2 EI network can approximate arbitrary mappings from  $\mathbb{R}^M$  to  $\mathbb{R}$ . For simplicity, we limit ourselves here to rank-2 networks and 1d outputs, which also results in stereotypical, non-overlapping spike trains (Fig. 5d). We contend that this is largely due to the simplicity of the 1d task, which should be remedied when considering higher-rank networks (see Discussion).

### 3 Noise-controlling versus noise-amplifying networks

Thus far, we have studied deterministic networks, and we have limited ourselves to rank-2 EI networks in which both populations share the same decoders (see Eq. (29)-Eq. (32)), i.e., excitatory neurons see the same inhibitory latent variable  $y^I$  as the inhibitory neurons themselves (and the same for the excitatory latent,  $y^E$ ). Here, we will show how relaxing this constraint and adding small amounts of noise to each neuron leads to networks that can control or amplify input-independent noise.

#### 3.1 Noise makes boundaries jitter

To study the addition of noise, we will begin by returning to the single, inhibitory population. Concretely, we assume that all neurons are subject to small independent white noise currents,  $\eta_i(t)$ , which we add to the differential equation, Eq. (1), of each neuron. This white noise will be filtered through the leaky integration of the membrane, so that the integrated voltage, Eq. (8), becomes

$$V_i = F_i x + E_i y + h * \eta(t) \leq T_i, \quad (48)$$

where  $h(\cdot)$  describes a one-sided exponential kernel, and “\*” denotes a convolution. Following Calaim et al. (2022), we move the noise term onto the threshold,

$$F_i x + E_i y \leq T_i - h * \eta(t), \quad (49)$$

and re-interpret this equation geometrically. From this view, the white noise causes random shifts in the precise position (but not the orientation) of a neuron’s boundary in input-output space (Fig. 6a). Additionally, and again following Calaim et al. (2022), we now consider neurons to have an additional self reset, following Eq. (26). This acts as a soft refractory period, and can be modeled as an additional threshold term

$$F_i x + E_i y \leq T_i - h * \eta(t) + \mu r_i(t), \quad (50)$$

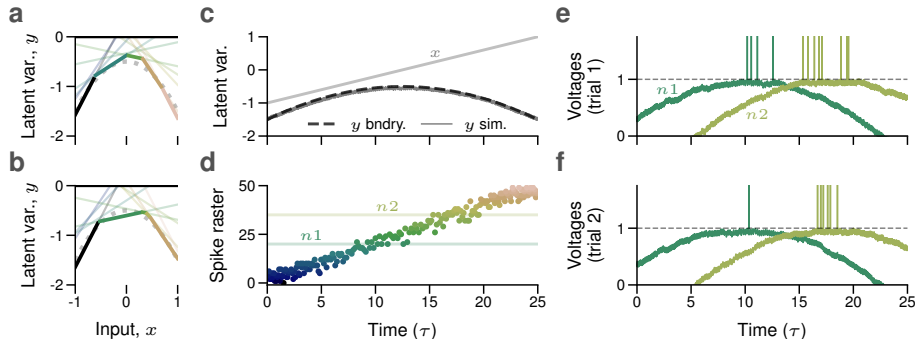


Figure 6: Noise causes jittery boundaries and irregular firing in the inhibitory population. **a,b**: Current noise makes individual neural threshold boundaries (faded colored lines) jitter up and down independently, resulting in a fluctuating population boundary (opaque multi-colored line) around the default boundary function (gray dashed line). The two panels (**a** and **b**) show two different realizations of noise and illustrate that each input value may be coded by a different neuron at different times. **c**: Input  $x$  and latent readout  $y$  for a simulation of a network with  $N = 50$  neurons, with a small amount of independent current noise added. **d**: Spike trains for the simulation in (**c**); note that several neurons become active for any given input  $x$ . **e,f**: Two trials from the network in (**c,d**). Note that the spike trains are variable despite the output  $y$  being reproduced precisely.

which increases the neuron’s threshold after spiking (recall that  $r_i(t)$  is the filtered spike train, see Eq. (4)). This can be considered as another mechanism that causes temporary shifts in the threshold of each neuron — in this case, the threshold will jump away from the population boundary by a fixed value after spiking, and exponentially decay back to its original location. At the network level, due to both of these effects, we can thus see that the boundaries of all neurons will jitter around their default positions, as illustrated for two noise snapshots in Fig. 6a,b, resulting in a noisy population boundary.

### 3.2 A jittery boundary causes irregular spiking

The key consequence of the jittery boundary is that more than one neuron can fire for a given input  $x$ . In the fully deterministic, inhibitory network, we saw that only one neuron becomes active for any given input  $x$ , compare Fig. 2d. However, once we add noise to the network, we observe instead that several neurons become active for any input value  $x$ , as shown in Fig. 6c-d.

Geometrically, the individual thresholds start fluctuating around their default position, and if a subset of neural thresholds are close to each other, then the noise and self-reset can push any of these thresholds to the front. As a consequence, neurons within this subset take turns in enforcing the boundary for any particular input value  $x$ . When the output  $y$  decays towards the boundary,

it reaches the threshold of the neuron that just happens to be more sensitive at that time point.

This type of redundancy can lead to neurons firing in a seemingly random fashion, simply because the latent variable  $y$  can reach one of several thresholds, depending on the noise in the system. Fig. 6e-f shows two trials of the inhibitory network. Just as in previous SCN work (Boerlin et al., 2013; Denève and Machens, 2016; Calaim et al., 2022), we see that the spike trains change from trial to trial. Firing patterns become more irregular if either the number of neurons in the network or the amplitude of the injected noise increases, until they become close to Poisson (not shown). However, even in this limit, the amount of injected noise needed is relatively small compared to the synaptic inputs, and so the spiking irregularity does not simply reflect large amounts of external noise. Strictly speaking, the input-output function for such a network is no longer deterministic, but should rather be described by a distribution  $p(y|x)$ , with a mean that is prescribed by a convex function from  $x$  to  $y$ .

### 3.3 Irregular firing amplifies noise in the decoder nullspace

The irregularity or noisiness of the individual spike trains of the network has important consequences for decoding. To visualize these consequences, we shift from the low-dimensional latent space back to the  $N$ -dimensional space spanned by the filtered spike trains or firing rates of the neurons,  $\mathbf{r} = (r_1, r_2, \dots, r_N)$ . We first observe that each neuron’s threshold also describes a hyperplane in firing rate space. When the voltage reaches the threshold, the terms of the neuron’s voltage equation (Eq. (50)) can be rewritten and solved for  $y$  as

$$y = \sum_{j=1}^N D_j r_j = \frac{T_i - h * \eta(t) + \mu r_i(t) - F_i x}{E_i}, \quad (51)$$

which defines a hyperplane with norm vector  $\mathbf{D} = (D_1, \dots, D_N)$  and offset as defined by the right-hand-side. The hyperplanes of different neurons have the same orientation, but different offsets. Two of these hyperplanes are shown in Fig. 7a for a two-neuron network.

The dynamics of the network can similarly be understood in this space. The firing rate vector,  $\mathbf{r}$ , will leak towards zero in the absence of spiking, compare Eq. (4). When it hits one of the thresholds, the respective neuron, say neuron  $k$ , fires, and updates the  $k$ -th firing rate. In the absence of noise, the firing rate vector will always hit the same neuron (Fig. 7a), eventually reaching a fixed point (Fig. 7b,c). However, when the neurons’ voltages are contaminated by noise, the thresholds randomly move around their default positions, and other neurons can eventually be the ones that fire (Fig. 7d). As a consequence, the firing rate vector starts to diffuse along the surfaces spanned by the neural thresholds (Fig. 7e).

By design, the readout given by  $\mathbf{D} = (D_1, \dots, D_N)$  is exactly orthogonal to this random diffusion (Fig. 7b,e), and is therefore largely unaffected by it (Fig. 7f). Indeed, the readout  $y$  only changes when the neural thresholds change,

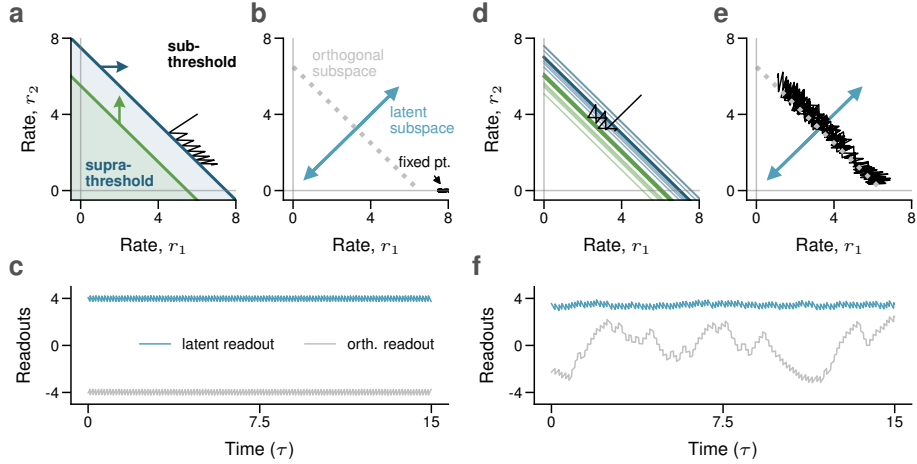


Figure 7: Irregular firing amplifies noise in the decoder nullspace. **a**: In the rank-1 network, all neural thresholds are parallel in firing rate space. For a deterministic network, only one of the neurons, here in blue, will fire, eventually reaching a fixed point. **b**: The latent readout subspace (blue) is orthogonal to the thresholds. The green dotted line shows the subspace orthogonal to the readout. **c**: Simulation of a deterministic network. Both readout and activity projected into the orthogonal subspace are noise-free. **d**: For a network contaminated by noise, the neural thresholds fluctuate in firing rate space. As a consequence, both the green and blue neuron participate in the dynamics. **e**: With both neurons taking random turns in firing, the dynamics diffuse along the orthogonal subspace. **f**: For the network with noise, the readout is no longer deterministic, but the noise is relatively small. In comparison, activity projected into the orthogonal subspace fluctuates wildly.

either through changes in the external inputs  $x$ , or, to a smaller extent, through the random fluctuations of the thresholds. However, if we project the neural activities onto a readout positioned in the orthogonal subspace, then we can see the large fluctuations from the random diffusion, which is caused by the random, irregular spiking of the neurons (Fig. 7f, green curve). The orthogonal readout will not pick up any changes in the signal caused by the signal  $x$ , and only see the random noise. We thus see that the recurrent connectivity of the network ensures that the desired decoder remains relatively independent of the noise generated by irregular activity, which will only appear in orthogonal directions. This result is similar to previous findings (Boerlin et al., 2013; Landau and Sompolinsky, 2021; DePasquale et al., 2023), and may also relate to controllability of network dynamics (Kao and Hennequin, 2019).

### 3.4 The rank-2 EI network is inhibition-stabilized and balanced

We now return to the coupled excitatory-inhibitory network, where we have one latent variable for the excitatory and one for the inhibitory population,  $y^E$  and  $y^I$ , respectively. We first consider a noisy version of the simple two-neuron setup from Fig. 4d, replacing each neuron by a population with  $N^E = 50$  and  $N^I = 50$  identical neurons, and adding a small amount of voltage noise (and self-reset) to each neuron, following Eq. (50). The boundary crossing in latent space remains unchanged (Fig. 8a), but is composed of two homogeneous populations. We then add one additional excitatory neuron (labelled  $E_2$ , Fig. 8a) with a different boundary, to illustrate how boundaries geometrically relate to voltage. Finally, to illustrate the inhibitory stabilization of the network, we consider the effect of a positive current stimulation to all neurons of the inhibitory population, a protocol that typically results in a “paradoxical effect” in inhibition-stabilized networks (Sadeh and Clopath, 2021). Such a stimulation shifts the inhibitory boundary upwards, and should result in a new steady state of the latent variable activity in which both populations have reduced activity (Fig. 8b).

We simulate this larger, noisier network, applying the inhibitory perturbation for the second half of the simulation time (Fig. 8c). We observe stable coding of the two latent variable readouts as predicted by the boundary crossing, with asynchronous irregular spiking activity. Furthermore, the stimulation of the inhibitory population causes a decrease in the activity of both populations, confirming the network as inhibition-stabilized. We note again that this relies upon our assumption that the inhibitory population is faster than the excitatory population (see Section 4 and Discussion). Next, by separating the positive and negative contributions to the voltage, we see that the synaptic inputs are roughly balanced, such that neurons in the network fire irregularly due to positive input fluctuations (Fig. 8c). Finally, the additional excitatory neuron,  $E_2$ , does not contribute to coding — its voltage remains hyperpolarized, with the relative amount of hyperpolarization being roughly proportional to the distance between its threshold and the current latent dynamics.

Overall, while these network dynamics may resemble cortical spiking activity, we stress that this comparison is somewhat limited in the case of the rank-2 EI network. Higher-rank systems will likely have additional mechanisms that promote irregularity and balance without requiring as much redundancy (see Discussion).

### 3.5 Cross-connections can suppress or amplify noise, and stability requires some level of noise control

In this last sub-section, we now finally consider the general case of the EI network where each population utilizes independent decoders to read out the latent variables. That is, in contrast to the previous shared decoder case in



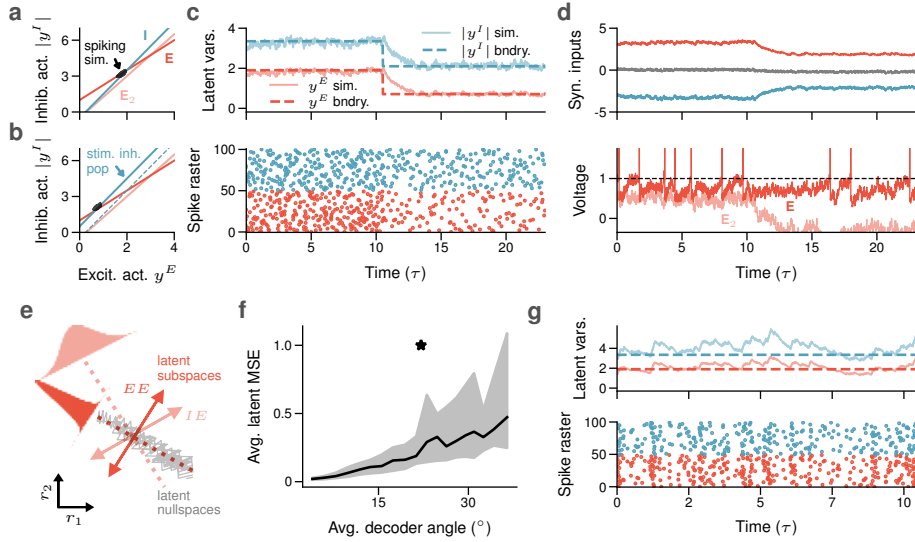


Figure 8: Irregular firing, balance, and noise control in the rank-2 EI network. **a**: Population boundaries for a homogeneous population of  $N^E = 50$  excitatory (E, red) and  $N^I = 50$  inhibitory (I, blue) neurons, with a stable boundary crossing, and one additional excitatory neuron with a different boundary ( $E_2$ , pink). **b**: When all neurons of the inhibitory population are stimulated, the boundary moves upward, shifting the fixed point to a new value, in which both readouts are reduced. **c**: Latent variable readouts (top) and spike rasters (bottom) of all neurons in the network over time, with the inhibitory population being stimulated at  $t = 10$ . **d**: Balanced inputs (top) and irregular spiking (bottom, red) for an example excitatory neuron from the homogeneous population, and the voltage of the additional excitatory neuron  $E_2$  (pink). **e**: Mistuning of decoders results in correlations between the nullspace of one population and the readout subspace of the other population. **f**: Decoding performance degrades as a function of decoder mismatch. **g**: Example simulation for misaligned decoders, resulting in more noise fluctuations compared to the aligned case.

Eq. (30) and Eq. (31), we now define the cross-connections as

$$W_{ij}^{IE} = E_i^{IE} D_j^{IE} \quad (52)$$

$$W_{ij}^{EI} = E_i^{EI} D_j^{EI}, \quad (53)$$

where  $D_j^{IE}$  and  $D_j^{EI}$  are potentially distinct from the self-decoders  $D_j^E$  and  $D_j^I$ , respectively. With this redefinition of Eq. (30) and Eq. (31), we are now looking at a rank-4 EI network, in which all cross- and self-connections can be arbitrary (sign-constrained) rank-1 matrices. The cross-connection matrices can now be “misaligned”, and so they will generally read out a mixture between each population’s own latent readouts,  $y^E$  and  $y^I$ , and the orthogonal subspace discussed above (Fig. 8e). To formalize these cross-connection readouts, we

introduce two new latent variables,

$$y^{IE} = \sum_{j=1}^{N^E} D_j^{IE} r_j^E \quad (54)$$

$$y^{EI} = \sum_{j=1}^{N^I} D_j^{EI} r_j^I. \quad (55)$$

These misaligned readouts can be explicitly split into a part that aligns with the self-decoders, and a part that captures noise from the null space. For example, let us focus on the excitatory readout of the inhibitory population. Writing  $\mathbf{D}^X = (D_1^X, \dots, D_N^X)$  for the vector of decoders for all four cases,  $X \in \{E, EI, IE, I\}$ , and assuming for simplicity that the four decoding vectors are normalized,  $(\mathbf{D}^X)^\top \mathbf{D}^X = 1$ , we obtain

$$y^{IE} = (\mathbf{D}^{IE})^\top \mathbf{r}^E \quad (56)$$

$$= (\mathbf{D}^{IE})^\top (\mathbf{D}^E (\mathbf{D}^E)^\top + \mathbf{I} - \mathbf{D}^E (\mathbf{D}^E)^\top) \mathbf{r}^E \quad (57)$$

$$= (\mathbf{D}^{IE})^\top \mathbf{D}^E y^E + \mathbf{D}^{IE\top} (\mathbf{I} - \mathbf{D}^E (\mathbf{D}^E)^\top) \mathbf{r}^E \quad (58)$$

$$= \alpha y^E + (\mathbf{D}^{IE} - \alpha \mathbf{D}^E)^\top \mathbf{r}^E. \quad (59)$$

Here, the first term captures a decreased readout of the correct excitatory latent,  $y^E$ , since  $\alpha = (\mathbf{D}^{IE})^\top \mathbf{D}^E \leq 1$ , and the equality sign only applies when  $\mathbf{D}^{IE} = \mathbf{D}^E$ . In turn, the second term captures the random fluctuations from the orthogonal subspace. As the decoders  $\mathbf{D}^{IE}$  and  $\mathbf{D}^E$  become less and less aligned,  $\alpha$  decreases and the relative power of signal and noise shifts towards noise (Fig. 8f,g; Landau and Sompolinsky (2021)). When the two readouts become orthogonal,  $\alpha = 0$ , and the inhibitory population receives no information about the correct latent,  $y^E$ , but only retrieves noise, the stability will be compromised (not shown).

## 4 Slow synapses, softer boundaries, and rate networks

Up to now we have studied an idealized spiking network model that ignores several basic properties of real neurons. Most notably, we have assumed that synaptic input currents are instantaneous, i.e., they arrive immediately and are infinitely short, and we have imposed that inhibitory neurons fire before excitatory neurons. As we will see, relaxing these assumptions will influence how sharp the boundary is and how accurately the input is mapped onto the output. In doing so, we arrive at a relationship between spiking dynamics and the smoothed, trial-averaged firing-rate dynamics that are typically studied in rate networks.

## 4.1 Slower synapses generate a finite boundary

First, we will examine how the boundary is affected when we change our assumptions about postsynaptic currents. For simplicity, we will first return to a single, rank-1 inhibitory population. Previously, we demonstrated that the dynamics of  $y$  are characterized by the combination of a leak and an infinitely steep boundary (compare Eq. (19), but assuming a one-dimensional input),

$$\dot{y} = -y + \sum_{i=1}^N D_i I(F_i x + E_i y - T_i). \quad (60)$$

For a fixed input  $x$ , we illustrate this infinitely steep boundary in Fig. 9a, where we plot  $y$  versus  $dy/dt$  (consider this as a vertical slice through Fig. 2a-c). The dynamics at the boundary are oscillatory, with leak dynamics, followed by instantaneous spiking (see Fig. 2d). In terms of the respective spike times,  $t_i^f$ , we can re-express the latent readout as (compare Eq. (14))

$$\dot{y} = -y + \sum_{i=1}^N \sum_f D_i \delta(t - t_i^f), \quad (61)$$

where  $t_i^f$  is the  $f$ -th spike fired by the  $i$ -th neuron. Here, the delta-function models the effect of a spike on the latent variable. Biophysically, the latent variable  $y$  is linearly related to the voltage (see Eq. (10)) and so the delta-function corresponds to an infinitely short, postsynaptic current.

In reality, of course, the postsynaptic current generated by a spike will last for a finite amount of time. We can explicitly include these synaptic dynamics by rewriting the voltage dynamics as

$$\dot{V}_i(t) = -V_i(t) + F_i c(t) + \sum_{j=1}^N W_{ij} \alpha_j(t), \quad (62)$$

where  $\alpha_j(t)$  is the series of postsynaptic currents due to neuron  $j$ . Two simple models of synaptic current dynamics are exponential decay and the square pulse (Gerstner et al., 2014). For a single spike at time  $t = 0$ , the exponential decay dynamics are given by

$$\alpha_j(t) = \frac{1}{\tau_s} \exp(-t/\tau_s), \quad (63)$$

and the square pulse by

$$\alpha_j(t) = \frac{1}{\tau_s} H(t) H(\tau_s - t), \quad (64)$$

and both are shown for two values of  $\tau_s$  in Fig. 9b, top. Here the synaptic time constant  $\tau_s$  is given in units of the membrane time constant, since  $\tau = 1$  in our case. Both equations scale  $\alpha_j$  with  $1/\tau_s$ , such that it always integrates to one,

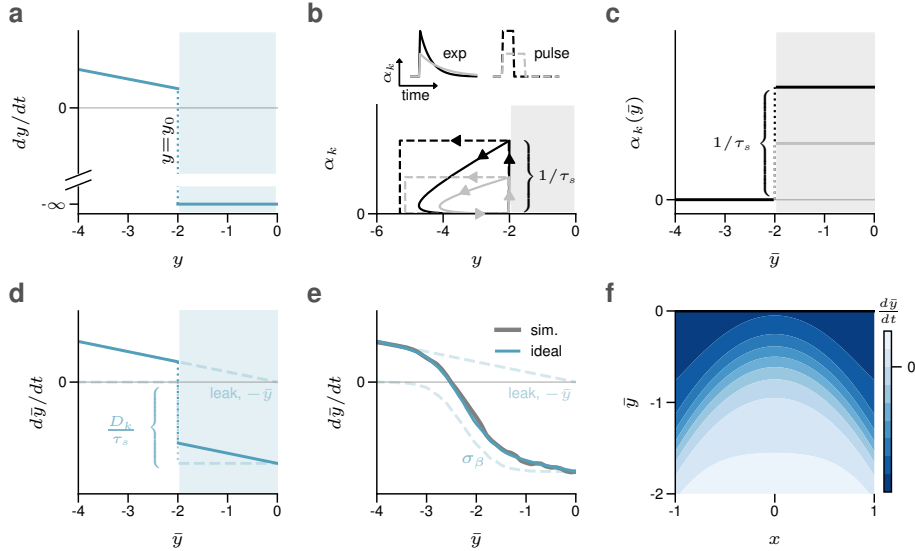


Figure 9: Hard and soft boundaries in the inhibitory population. **a**: Plot of latent  $y$  versus its derivative  $dy/dt$  for a synaptic delta-current. The threshold of the neuron sitting at  $y = y_0 = -2$  causes an infinitely steep boundary. **b**: Introduction of finite-time, exponential decay (solid lines) or square pulse (dashed lines) synaptic dynamics, with time constant  $\tau_s$  (shown for two values of  $\tau_s$  in gray and black); the resulting dynamics are oscillatory in  $(y, \alpha_k)$ -space, with jumps in  $\alpha_k$  of size  $1/\tau_s$ . **c**: Using the square pulse synapse model, the time-averaged dynamics of  $y$ , denoted  $\bar{y}$ , can be qualitatively approximated by assuming fixed synaptic input of amplitude  $1/\tau_s$  when the boundary is crossed (at  $\bar{y} = \bar{y}_0$ ), resulting in  $\alpha_k(\bar{y})$  as a scaled Heaviside function. **d**: The resulting plot of the average latent  $\bar{y}$  versus its derivative for the approximation to the square pulse synapse,  $\alpha_k(\bar{y})$ , from (c), where the jump in the derivative is scaled by  $D_k/\tau_s$ . **e**: Averaging the dynamics from (d) for a threshold jittering with white noise results in a soft, sigmoid-like boundary (gray, sim.). Trials were simulated with random initial conditions for  $y$  in the interval  $(-4, 4)$ . Comparison with an ‘ideal’ sigmoid function (blue), simulated as the average over the hard boundaries in (d) with Gaussian jitter. **f**: The soft boundary equivalent to the hard inhibitory network boundary from Fig. 2b-d and Fig. 6, in which neurons are arranged along a quadratic function.

and recovers the Dirac delta in the limit as  $\tau_s \rightarrow 0$ . Repeating the derivations in Sections 1.1-1.2, the latent dynamics becomes

$$\dot{y} = -y + \sum_{i=1}^N D_i \alpha_i(t). \quad (65)$$

We now consider a section of the boundary formed by one neuron, say neuron  $k$ , and visualize the dynamics in  $(y, \alpha_k)$ -space (Fig. 9b, bottom; again shown for

two values of  $\tau_s$ , black and gray, and for the two synapse models: exponential, solid lines, and square pulse, dashed lines). We see that the system relaxes into a steady-state oscillation at the boundary, with a regular spike pattern. However, the presence of the variable  $\alpha_k$  complicates the dynamical picture by adding another dimension, which will only grow in complexity when considering all  $N$  neurons and their respective synaptic variables.

To simplify the dynamics, we will aim to qualitatively describe a time-averaged approximation of  $y$ , which we will denote as  $\bar{y}$ , by replacing the temporal dynamics in  $\alpha_k(t)$  with a simple static function  $\alpha_k(\bar{y})$ . Consider, for instance, the square pulse synapse model, which only takes on one of two discrete values. Qualitatively, we see that  $\alpha_k$  sits at zero until the boundary is reached, when it jumps up to a non-zero value momentarily,  $\alpha_k \rightarrow 1/\tau_s$ , at which point  $y$  moves negatively back into the subthreshold area, until  $\alpha_k$  jumps back to zero. The time scale  $\tau_s$  affects mostly the size of the jump in  $\alpha_k$ , and less so the size of the change in  $y$ , which is bounded by  $D_k$  (if  $\tau_s \rightarrow 0$ ). We can therefore assume a functional form of  $\alpha_k$  as a scaled Heaviside function — it jumps up by  $1/\tau_s$  whenever the boundary is crossed, and jumps down to zero when  $y$  moves back into the subthreshold set (Fig. 9c; two values of  $\tau_s$  shown in black and gray). As a consequence, we will approximate each neuron's  $\alpha_i$  as

$$\alpha_i(\bar{y}) = \begin{cases} 1/\tau_s & \text{if } F_i x + E_i \bar{y} - T_i > 0 \\ 0 & \text{otherwise.} \end{cases} \quad (66)$$

Thus, we have effectively removed the history dependence of the synapses. Back at the level of the latent variable dynamics, we now have

$$\dot{\bar{y}} = -\bar{y} + \sum_{i=1}^N \frac{D_i}{\tau_s} H(F_i x + E_i \bar{y} - T_i). \quad (67)$$

We have thereby replaced the previously oscillatory dynamics at the boundary with a single fixed point, given when the boundary is reached (strictly speaking, the fixed point of the average dynamics does depend slightly on the time scale  $\tau_s$ , and will be different from the original  $y_0$ , but we have here ignored this effect for simplicity).

As illustrated in Fig. 9d, the infinitely steep boundary has become a finite-sized boundary. We can also see that the size of this boundary grows with the size of the decoder,  $D_k$ , and is inversely related to the timescale of the synaptic dynamics,  $\tau_s$ . Moreover, when we add a second, identical neuron to the picture, both neurons will fire two spikes per oscillation cycle, so that the effective size of the boundary doubles (not shown). More generally, the size of the boundary therefore scales linearly with the number of neurons at the boundary, as long as their thresholds are sufficiently closely spaced.

## 4.2 Noise causes a soft boundary

Let us next see how the boundary is affected when we add noise to the system. In Section 3, we saw that the main effect of voltage or current noise

was to randomly move the thresholds of the neurons. Similar effects can be obtained when synaptic weights or voltage resets slightly deviate from their idealized set points (Calaim et al., 2022).

In Fig. 9e, we simulated a neuron with normally-distributed threshold noise added and we plot the trial-averaged output against the trial-averaged derivative. With a slight abuse of notation, we will refer to this trial-averaged latent output as  $\bar{y}$  as well. We see that the main effect of the noise is to soften the boundary. Mathematically, the reason for this softening is that a Heaviside function with input subject to Gaussian noise takes the shape of the sigmoidal error function (erf). Due to its common use in rate networks and qualitative similarity to the error function, we choose to use the logistic function,

$$\sigma_{\beta}(u) = \frac{1}{1 + e^{-\beta u}}, \quad (68)$$

where the parameter  $\beta$  determines the steepness and is inversely proportional to the noise. For  $\beta \rightarrow \infty$ , we recover the deterministic Heaviside function. Apart from the parameters mentioned before—strength of the decoding weights, the inverse of the synaptic time scale, number of neurons around the boundary—the steepness of the boundary therefore also depends inversely on the level of the noise. When we now put this picture back into the full input-output,  $(x-y)$ -space as before, we can visualize the same network boundary as in Fig. 2b-d and Fig. 6, but now for the soft case, which is shown in Fig. 9f.

We thus have the following dynamics for the trial-averaged activity of a network with finite synaptic dynamics,

$$\dot{\bar{y}} = -\bar{y} + \sum_{i=1}^N \frac{D_i}{\tau_s} \sigma_{\beta}(F_i x + E_i \bar{y} - T_i). \quad (69)$$

This equation therefore describe the boundary by a single stable fixed point with locally asymmetric dynamics: fast attraction due to a steep boundary on one side and shallow attraction due to the leak on the other side (Fig. 9e). The slower the synapses and the larger the noise, the less strong this asymmetry becomes, until the notion of a boundary ceases to be useful in describing the system dynamics.

To illustrate this softer boundary at the population level, we simulated the network from Fig. 9f with the same setup from Fig. 6, but now with finite square-pulse synaptic dynamics ( $\tau_s = 0.5\tau$ , see Fig. 10a-c). We see that in this case, the latent readout still closely follows the threshold boundary (Fig. 10a), and the irregular firing and trial-to-trial variability are still retained (Fig. 10b,c). This demonstrates that the finite, soft boundary can still be geometrically visualized in the same way as the idealistic, infinite boundary from before, and that fragility issues previously associated with spike-coding networks (Chalk et al., 2016; Rullán Buxó and Pillow, 2020; Calaim et al., 2022) can be alleviated in this regime.

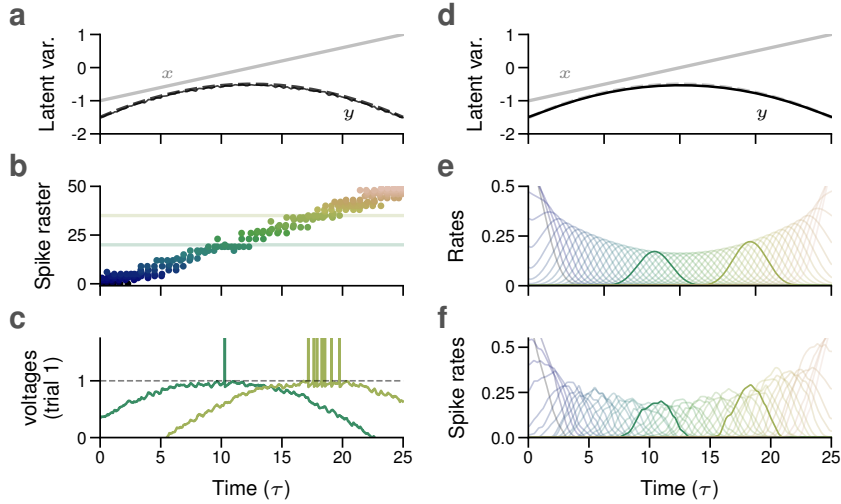


Figure 10: The inhibitory network with slow synapses. **a-c**: The network of  $N = 50$  neurons from Fig. 6 with slow synapses ( $\tau_s = 0.5\tau$ ) yields stable coding (a), irregular firing (b) and trial-to-trial variability (c). **d-f**: A rate version of the network also has stable coding (d) and has single-unit rate activities (e) that reproduce the trial-averaged activity of the spiking network (f; Gaussian-smoothed spikes for 100 trials of the system in (a)-(c)).

### 4.3 The latent variables of spiking and rate networks are equivalent

The dynamics of the trial-averaged latents has a simple relation to classical firing rate networks. Let us use the notation  $r_{F,i}$  to denote the activation of a unit  $i$  of a firing-rate network. Assuming a one-dimensional input  $x$ , the equation for an all-inhibitory rate network can be written as

$$\dot{r}_{F,i} = -r_{F,i} + \sigma(F_i x + \sum_j W_{ij} r_{F,j} - T_i), \quad (70)$$

where  $\sigma(\cdot)$  is the sigmoidal activation function of each neuron, here again modeled as a logistic function. Setting the inhibitory connection matrix to be rank-1,  $W_{ij} = E_i D_j$ , with  $D_j \leq 0$ , and defining the readout as  $y_F = \frac{1}{\tau_s} \sum_i D_i r_{F,i}$ , we can compute the derivative of  $y_F$  to obtain,

$$\dot{y}_F = -y_F + \sum_{i=1}^N \frac{D_i}{\tau_s} \sigma(F_i x + E_i y_F - T_i). \quad (71)$$

We note that this equation is identical to Eqs. (72) and (73), if we identify the readout  $y_F$  with the trial-averaged readout  $\bar{y}$  from the spiking network. Indeed, when we simulate this firing-rate version of the network, we see that it tracks

the boundary well, and the firing rates of the individual neurons closely match the trial-averaged rates of the spiking network (Fig. 10d-f).

Formally, we have therefore shown that the dynamics of the latent variables of a rank-1 (inhibitory) firing rate network are equivalent to the trial-averaged dynamics of a rank-1 (inhibitory) spiking network, as long as parameters are set such that the networks generate a clear boundary (see section 4.6 and Discussion).

#### 4.4 The EI boundaries become nullclines in the firing-rate limit

We now return to the rank-2 EI network, and consider the effect of slower synapses here. It is straightforward to take the arguments made above for the stable inhibitory boundary and carry them to the unstable excitatory boundary. This is illustrated for the two populations in Fig. 11a,b for a fixed input. The difference between the inhibitory and excitatory boundary is given by a simple flip of the boundary in the  $(|\bar{y}|, \dot{\bar{y}})$  plot (compare (Fig. 11a against Fig. 11b). Note that the output of the inhibitory population is negative in our convention (compare Fig. 9c), and we here plot its absolute value to allow better comparison with classical plots of EI networks.

When combining the two populations, we once more assume that they share the same decoders, following Eq. (29)-Eq. (32). Starting from Eq. (71), we then obtain the following equations for the trial-averaged dynamics,

$$\dot{\bar{y}}^I = -\bar{y}^I + \sum_{i=1}^{N^I} \frac{D_i^I}{\tau_s^I} \sigma(F_i^I x + E_i^{IE} \bar{y}^E + E_i^{II} \bar{y}^I - T_i^I) \quad (72)$$

$$\dot{\bar{y}}^E = -\bar{y}^E + \sum_{i=1}^{N^E} \frac{D_i^E}{\tau_s^E} \sigma(F_i^E x + E_i^{EE} \bar{y}^E + E_i^{EI} \bar{y}^I - T_i^E). \quad (73)$$

When comparing these equations with the original equation for the spiking network, Eqs. (37) and (38), we again see that we have simply replaced the indicator function  $I(\cdot)$  by a sigmoidal function,  $\sigma(\cdot)$ , divided by the time scales of the synaptic current pulses,  $\tau_s^I$  and  $\tau_s^E$ , respectively.

We illustrate these soft boundaries in the two-dimensional latent space,  $(|\bar{y}^I|, \bar{y}^E)$ , for homogeneous (or single neuron) populations in Fig. 11c,d. In turn, when setting the respective derivatives to zero, the boundaries become nullclines of the dynamics, as illustrated in Fig. 11e. We observe that the exact shapes and positions of the nullclines depend on the slope parameter  $\beta$  of the sigmoids, which approach the spiking boundaries (Fig. 11e, dotted lines) for large  $\beta$ . When we make the network heterogeneous, we can approximate each population's boundary as lying along a smooth convex (e.g., quadratic) function similar to Fig. 4f. Note that the shape of the boundary is now both determined by the individual neural thresholds, as well as the overall smoothness of the sigmoidal boundary (Fig. 11f).



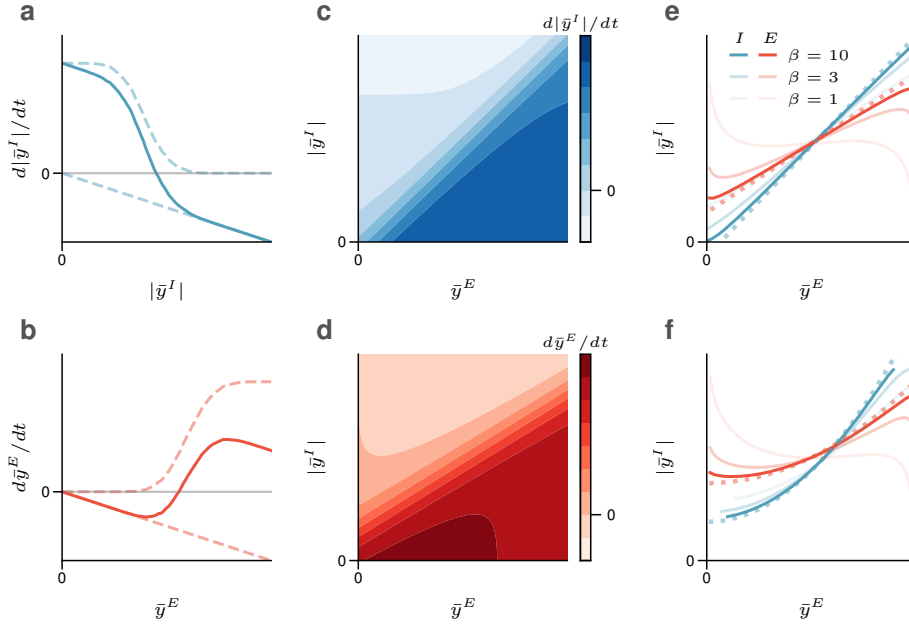


Figure 11: Dynamics of the rank-2 EI network with soft boundaries. **a**: Stable inhibitory dynamics, composed of a sigmoidal boundary and a leak. Replotted from Fig. 9e, using the absolute value of the inhibitory output,  $|\bar{y}^I|$ . **b**: Unstable excitatory dynamics, again composed of a sigmoidal boundary and a leak. **c-d**: The soft inhibitory and excitatory boundaries for the rank-2 EI network in 2d latent space (homogeneous populations). **e**: I and E nullclines of the homogeneous rate-based rank-2 EI system for three different values of  $\beta$ , controlling the slope of the sigmoids. The boundaries of the spike-based system are shown as dotted lines for comparison. **f**: I and E nullclines for a *heterogeneous* rank-2 EI system, in which neurons are arranged along quadratic functions as in Fig. 4c,f.

We illustrate the functionality of the rank-2 EI network with finite synapses by repeating the function approximation example from Fig. 5b-d. As illustrated in Fig. 12a, function approximation is made noisier with slowed-down synapses, but it is still reliable. While we no longer apply the ad hoc rule that inhibitory neurons fire first, the inhibitory synaptic dynamics should ideally be faster than the excitatory dynamics, in order to ensure stability (in this case  $\tau_E = \tau/4$  and  $\tau_I = \tau/10$ ; see Discussion).

Just as in the previous section, we can similarly derive the above equations by starting with a rank-2 firing rate network. When simulating such a network, we see that the latent readouts smoothly follow the intersection of the two boundaries, and rates will approximate the trial-averaged activities of the spiking network (Fig. 12b).

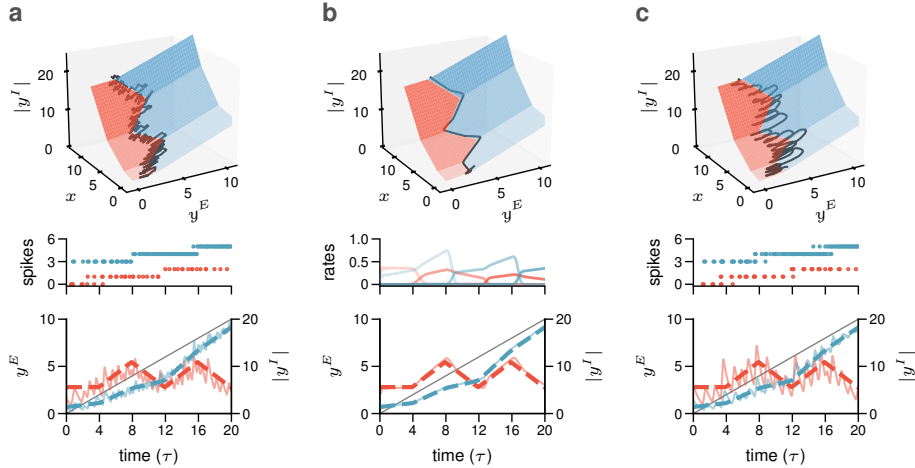


Figure 12: Function approximation in the rank-2 EI network with slow (spike-based) synapses and rate dynamics. **a**: The example from Fig. 5 with slow synapses ( $\tau_s^E = \tau/4$ ,  $\tau_s^I = \tau/10$ ) yields a somewhat reliable, yet noisier approximation to the boundary crossing. **b**: A rate-based version of the network with stable, reliable dynamics, and with rates that match the trial-averaged activity of the spiking network (not shown). **c**: Slowing down the inhibitory synapses sufficiently ( $\tau_s^E = \tau/4$ ,  $\tau_s^I = \tau/4$ ) leads to more oscillatory dynamics, with less reliable coding.

## 4.5 Synaptic time scales impact the accuracy of the output

Beyond making the boundary softer, the combination of mistuned network parameters and realistic synaptic currents can also influence the spiking dynamics and thereby the accuracy of the network’s input-output mapping. Recall that the output in the original network fluctuates between the threshold boundary and the reset boundary (see Fig. 2c). However, when synaptic currents are not instantaneous, and when the thresholds are not fixed, then the output can sometimes cross multiple thresholds, and multiple neurons fire. In this case, the output  $y$  does not simply bounce back to the reset boundary, but moves further into the subthreshold regime. This will be especially true if the synaptic time constants are very slow, or if there are significant delays in axonal conductance. These resulting oscillatory effects in  $y$  decrease the accuracy with which the input is mapped onto the output. An example is shown in Fig. 12c, in which  $\tau_s^E = \tau_s^I = \tau/4$ . From a computational perspective, this loss of accuracy is not desirable. From a biological perspective, the simultaneous crossing of multiple thresholds causes strong, synchronous firing, which may relate to oscillatory dynamics in the brain (Chalk et al., 2016). However, these effects should also be mitigated in higher-rank networks (see Discussion).

## 4.6 The spike-rate equivalence requires a latent boundary

We note that the above derivations are restricted to networks that have a block-wise rank-1 structure, i.e., in which both self-connectivity and cross-connectivity of the excitatory and inhibitory subnetworks is rank-1. However, not all networks with this structure will permit a transition from spiking to rate networks as described here.

First, we have assumed that the cross-connections have the same decoders as the self-connections of each population (compare Eqs. (29) and (32)). As explained in Section 3, when the cross-connections are not aligned, the spiking network will accumulate noise, and a match between trial-averaged spiking networks and rate networks can no longer be guaranteed. This restriction on cross-connection alignment is usually not followed in the design of firing rate networks.

Second, parameters in classical firing rate networks are usually chosen such that individual neurons operate in the full regime of their input function, from below threshold to large firing rates and even into saturation. The underlying reason is always that the neural activation functions serve as basis of an underlying function approximation scheme (compare Fig. 1a–c). Apart from feedforward networks, examples include line attractor networks in which neural thresholds are staggered in latent space so that the addition of all neural activation functions precisely counters the leak (Seung, 1996; Eliasmith and Anderson, 2003), or decision-making models that use saturation to obtain bistability (Mastrogiuseppe and Ostojic, 2018).

In contrast, in the spiking networks here, neural thresholds are aligned in latent space such that they join to form a boundary. As a consequence, each neuron touches the boundary at some point, and its activation function enforces the boundary. Indeed, parameters need to be chosen such that the boundary is so steep as to be basically unsurmountable by the latent variable. The boundary becomes particularly steep when the synaptic currents,  $\tau_s$ , become sufficiently short. Apart from that constraint, the precise shape of the boundary function does not matter.

Importantly, this operating regime is crucial in order to obtain balanced synaptic current inputs into the neurons (compare Fig. 1d,e). In the rate-domain, our perspective bears a resemblance to other rate-based models featuring non-saturating nonlinearities (Miller and Troyer, 2002; Hansel and van Vreeswijk, 2002; Ahmadian et al., 2013; Rubin et al., 2015; Hennequin et al., 2018). Indeed, we would reinterpret the respective neural activation functions as implementing soft boundaries.

## 5 Discussion

In this article, we have proposed a new framework for understanding a broad class of spiking neural network models based on spike-threshold boundaries. These boundaries come from the inherent inequality at the core of each neuron

— the voltage threshold — which triggers a spike. Classic approaches usually seek to eliminate the threshold inequality by, e.g., filtering or averaging spike trains, and to replace it with a continuous activation function (Dayan and Abbott, 2005; Gerstner et al., 2014). We take a different approach here. By defining a one-dimensional latent variable readout, we show that the spike-threshold boundaries of rank-1 networks can be visualized in input-output space, with each neuron forming a linear boundary. A population of neurons forms a convex boundary delineating subthreshold from suprathreshold areas, and for an inhibitory population this boundary forms a stable input-output function. For an excitatory population, the boundary is instead unstable, but can then be stabilized in a coupled EI network, where the dynamics sit at the crossing of the two boundaries. The boundary between sub- and supra-threshold regimes thus becomes the center of spike-based computation, and distinct from the “feature detector” perspective (Fig. 1).

The mathematics of systems with inequalities and hard boundaries has a rich history in constrained convex and non-convex optimization (Boyd and Vandenberghe, 2004). Previous work on spike coding has demonstrated how the dynamics of spiking networks can be mapped onto convex optimization problems such as quadratic programming (Barrett et al., 2013; Mancoo et al., 2020), yielding stable, convex input-output transformations. We extended this work here by showing that coupled EI networks are capable of non-convex function approximation, with links to difference of convex (DC) programming (Horst and Thoai, 1999; Lipp and Boyd, 2016). Similarly, previous work has linked EI networks to minimax optimization (Seung et al., 1997; Li and Pehlevan, 2020), but with a focus more on attractor dynamics rather than function approximation. Overall, the analogy between spiking thresholds and constraint boundaries offers a fruitful perspective that may lead to new insights and algorithms that harness the power of convex optimization (Boyd and Vandenberghe, 2004). Moreover, such techniques have recently caught on in deep learning in the form of deep implicit layers, offering potential avenues for learning and scaling up our framework (Amos and Kolter, 2017; Gould et al., 2021).

In the work presented here we limited ourselves to small populations of neurons with rank-1 connectivity. Though increasing the number of neurons in rank-1 (or rank-2 EI) networks may enable closer and closer approximations to arbitrary continuous 1-d functions, the  $N \rightarrow \infty$  limit of rank-1 networks is likely too limiting to relate to biological spiking networks. Furthermore, though we do not demonstrate it here, this larger-scale limit requires the absence of noise and communication delays, in addition to having very large synaptic input currents. Instead, to stay within a biologically realistic and workable regime, scaling up the number of neurons should coincide with scaling up the rank of the connectivity (Calaim et al., 2022). Fortunately, many of the intuitions about spike thresholds and convex boundaries transfer to the higher-dimensional input-output spaces of arbitrary rank-K networks. Furthermore, many signatures of biological activity regimes discussed here, such as irregular firing and balance, become more robust in this higher-dimensional regime (Calaim et al., 2022).

The rank-1 and rank-2 spiking networks studied here can be seen as a partic-

ular generalization of spike-coding networks (SCNs) (Boerlin et al., 2013; Denève and Machens, 2016), with the spike-threshold boundary being a generalization of the concept of a bounding box put forward in Calaim et al. (2022). As we demonstrate, this generalization frees SCNs from the constraint of linear computation without evoking dendritic or synaptic nonlinearities (Thalmeier et al., 2016; Alemi et al., 2018; Nardin et al., 2021; Mikulasch et al., 2021). Many of the desirable biological properties of SCNs are preserved here, including robustness, firing irregularity, and E/I balance. We can reinterpret the bounding box as being composed of two components — local regions of the boundary are stable, with lateral inhibition between neurons, but globally the closed nature of the box may lead to errant positive feedback and thus fragility in the form of epileptic (“ping-pong”) behavior (Chalk et al., 2016; Rullán Buxó and Pillow, 2020; Calaim et al., 2022). Our framework eliminates this previous limitation, fully separating the positive and negative feedback loops in the network. Taking into account slower synapses with delays, we are able to relate our work to the dynamics of rate networks, similar to previous approaches (Kadmon et al., 2020; Rullán Buxó and Pillow, 2020). However, our aim here is not to emulate a rate-based system with spikes, but rather to demonstrate the relationship between hard spike boundaries and soft rate boundaries.

One major biological implication of our work is the natural distinction between excitatory and inhibitory populations. Many previous models, in contrast, typically start with Dale’s law as a biological constraint, then attempt to achieve performance on par with an unconstrained network, and finally reflect on the potential benefits of such a constraint for, e.g., stability or robustness (Hennequin et al., 2014; Song et al., 2016; Brendel et al., 2020; Cornford et al., 2020; Haber and Schneidman, 2022). Our framework instead puts forth a particular computational role for Dale’s law — it is the combination of positive feedback from the unstable excitatory boundary with negative feedback from the stable inhibitory boundary that enables flexible input-output mappings. This idea is reminiscent of so-called mixed feedback systems in control theory, which are beginning to be explored in the neuroscience domain (Sepulchre et al., 2019; Sepulchre, 2022). In addition to the unique computational role of Dale’s law in our model, the separation into excitatory and inhibitory populations also links the dynamical behavior of our model to previous work on EI networks, including inhibition-stabilized networks (Sadeh and Clopath, 2021).

A strict requirement of the rank-2 EI networks that we study is that inhibition should be faster than excitation in order to keep the dynamics tightly around the intersection of the two boundaries. While some evidence suggests that the synaptic time constant of inhibition may be slower than that of excitation (e.g., see discussion in Fourcaud and Brunel (2002)), other factors, such as the localization of inhibitory synapses close to the peri-somatic zone (Freund and Katona, 2007), or the cortical connectivity patterns (short-range for inhibition, long-range for excitation) suggest that inhibition could also be faster than excitation.

Overall, our work can be seen as a bridge between mechanistic and functional network models of the brain. Mechanistic models, perhaps best represented by

balanced spiking networks (Van Vreeswijk and Sompolinsky, 1996; Amit and Brunel, 1997; Brunel, 2000), capture many important features of cortical dynamics, including asynchronous irregular activity, excitation-inhibition balance, and correlated neural variability (Vogels and Abbott, 2005; Renart et al., 2010; Rosenbaum et al., 2017; Huang et al., 2019). However, such models, and especially their theoretical analysis, have typically been limited to linear computations in large networks (infinitely many neurons in the mean-field limit, or 1000-10000 in practice). In contrast, our work focuses on non-linear computations in much smaller spiking networks (5-50 neurons).

While various ways have been proposed to obtain non-linear computations in the mean-field limit (Renart et al., 2007; Roudi and Latham, 2007; Hansel and Mato, 2013; Lajoie et al., 2016; Ingrosso and Abbott, 2019; Kim and Chow, 2021), one recent study parallels our work in several interesting ways. Baker et al. (2020) utilize networks with “semi-balance” or “approximate balance” in order to achieve nonlinear computation. Notably, they observe that active subpopulations retain balanced input, whereas others are hyperpolarized. Despite the size differences, this is precisely what our networks predict as well (Fig. 8d), and so there may be a new route to understand semi-balanced networks. More generally, this supports the notion that balance must be broken or loose enough to enable nonlinear computations (Ahmadian and Miller, 2021).

Functional models of static input-output mappings are perhaps best represented by feedforward rate networks (Hunsberger and Eliasmith, 2015; Yamins and DiCarlo, 2016). However, such networks do not agree with the heavily recurrent connections found in the brain, they do not obey Dale’s law, and they rely on neurons being feature detectors, which conflicts with the idea of balanced inputs (Fig. 1). Here we have shown that function approximation can also be achieved in (low-rank) recurrent networks obeying Dale’s law, and with balanced inputs. Typically, the study of low-rank networks has emphasized the generation of internal dynamics for decision making, memory, and motor control (Eliasmith, 2005; Mastrogiuseppe and Ostojic, 2018; Dubreuil et al., 2022). Though we have deliberately ignored dynamics here, some simple dynamical motifs such as bistability can be achieved even in the rank-2 EI network provided that there are multiple boundary crossings (not explored here). Higher-dimensional systems can have much richer dynamics in the latent space, as is already known from work on rate networks, and will be explored in future work. One aspect of dynamics that we do consider in this work is the existence of noise-amplifying or noise-suppressing connectivities. These properties have also been described in other low-rank networks (Landau and Sompolinsky, 2018, 2021; DePasquale et al., 2023).

Advances in learning algorithms have led to an explosion of research on training functional spiking network models (Abbott et al., 2016; Neftci et al., 2019). Interestingly, many algorithms smooth over the spike-threshold nonlinearity using “surrogate” or pseudo-gradients (Bellec et al., 2018; Neftci et al., 2019; Zenke and Vogels, 2021), or directly train on rate dynamics (DePasquale et al., 2023), which may smooth out or prevent the development of well-formed latent boundaries. It will be interesting to develop scalable training algorithms

for the networks discussed here, and to see how additional constraints during training may affect the development of spike-threshold boundaries.

In summary, our framework offers a new perspective on spike-based computation. It offers the potential to better understand the computational regimes and benefits of the balanced state as observed in cortex, as well as a new tool to analyze the computations of other models, such as trained networks. Furthermore, the perspective itself may be useful in developing novel spiking algorithms, such as those based on constrained optimization and implicit input-output transformations. Finally, while the potential to scale up the framework to higher-rank networks with dynamical computations is still to be demonstrated, it may serve as a promising direction for scalable computation with spikes.

## Acknowledgements

We thank Alfonso Renart, Francesca Mastrogiuseppe, and Sander Keemink for detailed comments on the manuscript. We thank all members of the Machens Lab for helpful discussions and feedback, especially Allan Mancoo for discussions on convex optimization, and Bertrand Lacoste for discussions pertaining to decomposition into the difference of two convex functions. This work was supported by the Fundação para a Ciência e a Tecnologia (project FCT-PTDC/BIA-OUT/ 32077/ 2017-IC&DT-LISBOA-01-0145-FEDER) and by the Simons Foundation (Simons Collaboration on the Global Brain #543009).

## References

- Abbott, L. F., DePasquale, B., and Memmesheimer, R.-M. (2016). Building functional networks of spiking model neurons. *Nature neuroscience*, 19(3):350–355.
- Ahmadian, Y. and Miller, K. D. (2021). What is the dynamical regime of cerebral cortex? *Neuron*, 109(21):3373–3391.
- Ahmadian, Y., Rubin, D. B., and Miller, K. D. (2013). Analysis of the stabilized supralinear network. *Neural computation*, 25(8):1994–2037.
- Alemi, A., Machens, C., Deneve, S., and Slotine, J.-J. (2018). Learning nonlinear dynamics in efficient, balanced spiking networks using local plasticity rules. In *Proceedings of the AAAI Conference on Artificial Intelligence*, volume 32.
- Almog, M. and Korngreen, A. (2016). Is realistic neuronal modeling realistic? *Journal of neurophysiology*, 116(5):2180–2209.
- Amit, D. J. and Brunel, N. (1997). Model of global spontaneous activity and local structured activity during delay periods in the cerebral cortex. *Cerebral cortex (New York, NY: 1991)*, 7(3):237–252.

- Amos, B. and Kolter, J. Z. (2017). Optnet: Differentiable optimization as a layer in neural networks. In *International Conference on Machine Learning*, pages 136–145. PMLR.
- Baker, C., Zhu, V., and Rosenbaum, R. (2020). Nonlinear stimulus representations in neural circuits with approximate excitatory-inhibitory balance. *PLoS computational biology*, 16(9):e1008192.
- Barak, O. (2017). Recurrent neural networks as versatile tools of neuroscience research. *Current opinion in neurobiology*, 46:1–6.
- Barrett, D. G., Denève, S., and Machens, C. K. (2013). Firing rate predictions in optimal balanced networks. *Advances in Neural Information Processing Systems*, 26.
- Barrett, D. G., Deneve, S., and Machens, C. K. (2016). Optimal compensation for neuron loss. *Elife*, 5:e12454.
- Bellec, G., Salaj, D., Subramoney, A., Legenstein, R., and Maass, W. (2018). Long short-term memory and learning-to-learn in networks of spiking neurons. *Advances in neural information processing systems*, 31.
- Bernáez Timón, L., Ekelmans, P., Kravnyukova, N., Rose, T., Busse, L., and Tchumatchenko, T. (2022). How to incorporate biological insights into network models and why it matters. *The Journal of Physiology*.
- Boerlin, M., Machens, C. K., and Denève, S. (2013). Predictive coding of dynamical variables in balanced spiking networks. *PLoS computational biology*, 9(11):e1003258.
- Boyd, S. P. and Vandenberghe, L. (2004). *Convex optimization*. Cambridge university press.
- Brendel, W., Bourdoukan, R., Vertech, P., Machens, C. K., and Denève, S. (2020). Learning to represent signals spike by spike. *PLoS computational biology*, 16(3):e1007692.
- Brunel, N. (2000). Dynamics of sparsely connected networks of excitatory and inhibitory spiking neurons. *Journal of computational neuroscience*, 8:183–208.
- Calaim, N., Dehmelt, F. A., Gonçalves, P. J., and Machens, C. K. (2022). The geometry of robustness in spiking neural networks. *Elife*, 11:e73276.
- Chalk, M., Gutkin, B., and Deneve, S. (2016). Neural oscillations as a signature of efficient coding in the presence of synaptic delays. *Elife*, 5:e13824.
- Chung, S. and Abbott, L. (2021). Neural population geometry: An approach for understanding biological and artificial neural networks. *Current opinion in neurobiology*, 70:137–144.



- Cimesa, L., Ciric, L., and Ostojic, S. (2022). Geometry of population activity in spiking networks with low-rank structure. *bioRxiv*, pages 2022–11.
- Cornford, J., Kalajdzievski, D., Leite, M., Lamarquette, A., Kullmann, D. M., and Richards, B. (2020). Learning to live with dale’s principle: Anns with separate excitatory and inhibitory units. *bioRxiv*, pages 2020–11.
- Cunningham, J. P. and Yu, B. M. (2014). Dimensionality reduction for large-scale neural recordings. *Nature neuroscience*, 17(11):1500–1509.
- Dayan, P. and Abbott, L. F. (2005). *Theoretical neuroscience: computational and mathematical modeling of neural systems*. MIT press.
- Denève, S. and Machens, C. K. (2016). Efficient codes and balanced networks. *Nature neuroscience*, 19(3):375–382.
- DePasquale, B., Sussillo, D., Abbott, L., and Churchland, M. M. (2023). The centrality of population-level factors to network computation is demonstrated by a versatile approach for training spiking networks. *Neuron*.
- Dubreuil, A., Valente, A., Beiran, M., Mastrogiuseppe, F., and Ostojic, S. (2022). The role of population structure in computations through neural dynamics. *Nature neuroscience*, 25(6):783–794.
- Eccles, J. C. (1976). From electrical to chemical transmission in the central nervous system: the closing address of the sir henry dale centennial symposium cambridge, 19 september 1975. *Notes and records of the Royal Society of London*, 30(2):219–230.
- Eliasmith, C. (2005). A unified approach to building and controlling spiking attractor networks. *Neural computation*, 17(6):1276–1314.
- Eliasmith, C. and Anderson, C. H. (2003). *Neural engineering: Computation, representation, and dynamics in neurobiological systems*. MIT press.
- Eliasmith, C. and Trujillo, O. (2014). The use and abuse of large-scale brain models. *Current opinion in neurobiology*, 25:1–6.
- Fourcaud, N. and Brunel, N. (2002). Dynamics of the firing probability of noisy integrate-and-fire neurons. *Neural computation*, 14(9):2057–2110.
- Freund, T. F. and Katona, I. (2007). Perisomatic inhibition. *Neuron*, 56(1):33–42.
- Fusi, S., Miller, E. K., and Rigotti, M. (2016). Why neurons mix: high dimensionality for higher cognition. *Current opinion in neurobiology*, 37:66–74.
- Gallego, J. A., Perich, M. G., Miller, L. E., and Solla, S. A. (2017). Neural manifolds for the control of movement. *Neuron*, 94(5):978–984.

- Gerstner, W., Kistler, W. M., Naud, R., and Paninski, L. (2014). *Neuronal dynamics: From single neurons to networks and models of cognition*. Cambridge University Press.
- Gould, S., Hartley, R., and Campbell, D. (2021). Deep declarative networks. *IEEE Transactions on Pattern Analysis and Machine Intelligence*, 44(8):3988–4004.
- Haber, A. and Schneidman, E. (2022). The computational and learning benefits of daleian neural networks. *arXiv preprint arXiv:2210.05961*.
- Haider, B., Duque, A., Hasenstaub, A. R., and McCormick, D. A. (2006). Neocortical network activity in vivo is generated through a dynamic balance of excitation and inhibition. *Journal of Neuroscience*, 26(17):4535–4545.
- Hansel, D. and Mato, G. (2013). Short-term plasticity explains irregular persistent activity in working memory tasks. *Journal of Neuroscience*, 33(1):133–149.
- Hansel, D. and van Vreeswijk, C. (2002). How noise contributes to contrast invariance of orientation tuning in cat visual cortex. *Journal of Neuroscience*, 22(12):5118–5128.
- Hartman, P. (1959). On functions representable as a difference of convex functions. *Pacific Journal of Mathematics*, 9(3):707–713.
- Hennequin, G., Ahmadian, Y., Rubin, D. B., Lengyel, M., and Miller, K. D. (2018). The dynamical regime of sensory cortex: stable dynamics around a single stimulus-tuned attractor account for patterns of noise variability. *Neuron*, 98(4):846–860.
- Hennequin, G., Vogels, T. P., and Gerstner, W. (2014). Optimal control of transient dynamics in balanced networks supports generation of complex movements. *Neuron*, 82(6):1394–1406.
- Horst, R. and Thoai, N. V. (1999). Dc programming: overview. *Journal of Optimization Theory and Applications*, 103:1–43.
- Huang, C., Ruff, D. A., Pyle, R., Rosenbaum, R., Cohen, M. R., and Doiron, B. (2019). Circuit models of low-dimensional shared variability in cortical networks. *Neuron*, 101(2):337–348.
- Hunsberger, E. and Eliasmith, C. (2015). Spiking deep networks with lif neurons. *arXiv preprint arXiv:1510.08829*.
- Ingroso, A. and Abbott, L. (2019). Training dynamically balanced excitatory-inhibitory networks. *PloS one*, 14(8):e0220547.
- Izhikevich, E. M. (2007). *Dynamical systems in neuroscience*. MIT press.

- Jazayeri, M. and Ostojic, S. (2021). Interpreting neural computations by examining intrinsic and embedding dimensionality of neural activity. *Current opinion in neurobiology*, 70:113–120.
- Kadmon, J., Timcheck, J., and Ganguli, S. (2020). Predictive coding in balanced neural networks with noise, chaos and delays. *Advances in neural information processing systems*, 33:16677–16688.
- Kao, T.-C. and Hennequin, G. (2019). Neuroscience out of control: control-theoretic perspectives on neural circuit dynamics. *Current opinion in neurobiology*, 58:122–129.
- Keemink, S. W. and Machens, C. K. (2019). Decoding and encoding (de)mixed population responses. *Current Opinion in Neurobiology*, 58:112–121.
- Kim, C. M. and Chow, C. C. (2021). Training spiking neural networks in the strong coupling regime. *Neural computation*, 33(5):1199–1233.
- Lajoie, G., Lin, K. K., Thivierge, J.-P., and Shea-Brown, E. (2016). Encoding in balanced networks: Revisiting spike patterns and chaos in stimulus-driven systems. *PLoS computational biology*, 12(12):e1005258.
- Landau, I. D. and Sompolinsky, H. (2018). Coherent chaos in a recurrent neural network with structured connectivity. *PLoS computational biology*, 14(12):e1006309.
- Landau, I. D. and Sompolinsky, H. (2021). Macroscopic fluctuations emerge in balanced networks with incomplete recurrent alignment. *Physical Review Research*, 3(2):023171.
- Langdon, C., Genkin, M., and Engel, T. A. (2023). A unifying perspective on neural manifolds and circuits for cognition. *Nature Reviews Neuroscience*, pages 1–15.
- Li, P., Cornford, J., Ghosh, A., and Richards, B. (2023). Learning better with dale’s law: A spectral perspective. *bioRxiv*, pages 2023–06.
- Li, Q. and Pehlevan, C. (2020). Minimax dynamics of optimally balanced spiking networks of excitatory and inhibitory neurons. *Advances in Neural Information Processing Systems*, 33:4894–4904.
- Lindsay, G. W. (2021). Convolutional neural networks as a model of the visual system: Past, present, and future. *Journal of cognitive neuroscience*, 33(10):2017–2031.
- Lipp, T. and Boyd, S. (2016). Variations and extension of the convex–concave procedure. *Optimization and Engineering*, 17:263–287.
- Mancoo, A., Keemink, S., and Machens, C. K. (2020). Understanding spiking networks through convex optimization. *Advances in Neural Information Processing Systems*, 33:8824–8835.

- Martin, K. A. (1994). A brief history of the “feature detector”. *Cerebral cortex*, 4(1):1–7.
- Mastrogiuseppe, F. and Ostojic, S. (2018). Linking connectivity, dynamics, and computations in low-rank recurrent neural networks. *Neuron*, 99(3):609–623.
- Miconi, T. (2017). Biologically plausible learning in recurrent neural networks reproduces neural dynamics observed during cognitive tasks. *Elife*, 6:e20899.
- Mikulasch, F. A., Rudelt, L., and Priesemann, V. (2021). Local dendritic balance enables learning of efficient representations in networks of spiking neurons. *Proceedings of the National Academy of Sciences*, 118(50):e2021925118.
- Miller, K. D. and Troyer, T. W. (2002). Neural noise can explain expansive, power-law nonlinearities in neural response functions. *Journal of neurophysiology*, 87(2):653–659.
- Nardin, M., Phillips, J. W., Podlaski, W. F., and Keemink, S. W. (2021). Nonlinear computations in spiking neural networks through multiplicative synapses. *Peer Community Journal*, 1.
- Neftci, E. O., Mostafa, H., and Zenke, F. (2019). Surrogate gradient learning in spiking neural networks: Bringing the power of gradient-based optimization to spiking neural networks. *IEEE Signal Processing Magazine*, 36(6):51–63.
- Parisien, C., Anderson, C. H., and Eliasmith, C. (2008). Solving the problem of negative synaptic weights in cortical models. *Neural computation*, 20(6):1473–1494.
- Renart, A., De La Rocha, J., Bartho, P., Hollender, L., Parga, N., Reyes, A., and Harris, K. D. (2010). The asynchronous state in cortical circuits. *science*, 327(5965):587–590.
- Renart, A., Moreno-Bote, R., Wang, X.-J., and Parga, N. (2007). Mean-driven and fluctuation-driven persistent activity in recurrent networks. *Neural computation*, 19(1):1–46.
- Rockafellar, R. T. (1997). *Convex analysis*, volume 11. Princeton university press.
- Rosenbaum, R., Smith, M. A., Kohn, A., Rubin, J. E., and Doiron, B. (2017). The spatial structure of correlated neuronal variability. *Nature neuroscience*, 20(1):107–114.
- Roudi, Y. and Latham, P. E. (2007). A balanced memory network. *PLoS computational biology*, 3(9):e141.
- Rubin, D. B., Van Hooser, S. D., and Miller, K. D. (2015). The stabilized supra-linear network: a unifying circuit motif underlying multi-input integration in sensory cortex. *Neuron*, 85(2):402–417.

- Rullán Buxó, C. E. and Pillow, J. W. (2020). Poisson balanced spiking networks. *PLoS computational biology*, 16(11):e1008261.
- Sadeh, S. and Clopath, C. (2021). Inhibitory stabilization and cortical computation. *Nature Reviews Neuroscience*, 22(1):21–37.
- Saxena, S. and Cunningham, J. P. (2019). Towards the neural population doctrine. *Current opinion in neurobiology*, 55:103–111.
- Sepulchre, R. (2022). Spiking control systems. *Proceedings of the IEEE*.
- Sepulchre, R., Drion, G., and Franci, A. (2019). Control across scales by positive and negative feedback. *Annual Review of Control, Robotics, and Autonomous Systems*, 2:89–113.
- Seung, H. S. (1996). How the brain keeps the eyes still. *Proceedings of the National Academy of Sciences*, 93(23):13339–13344.
- Seung, H. S., Richardson, T., Lagarias, J., and Hopfield, J. J. (1997). Minimax and hamiltonian dynamics of excitatory-inhibitory networks. *Advances in neural information processing systems*, 10.
- Shadlen, M. N. and Newsome, W. T. (1998). The variable discharge of cortical neurons: implications for connectivity, computation, and information coding. *Journal of neuroscience*, 18(10):3870–3896.
- Shao, Y. and Ostojic, S. (2023). Relating local connectivity and global dynamics in recurrent excitatory-inhibitory networks. *PLOS Computational Biology*, 19(1):e1010855.
- Shenoy, K. V., Sahani, M., and Churchland, M. M. (2013). Cortical control of arm movements: a dynamical systems perspective. *Annual review of neuroscience*, 36:337–359.
- Softky, W. R. and Koch, C. (1993). The highly irregular firing of cortical cells is inconsistent with temporal integration of random epsps. *Journal of neuroscience*, 13(1):334–350.
- Song, H. F., Yang, G. R., and Wang, X.-J. (2016). Training excitatory-inhibitory recurrent neural networks for cognitive tasks: a simple and flexible framework. *PLoS computational biology*, 12(2):e1004792.
- Sussillo, D. (2014). Neural circuits as computational dynamical systems. *Current opinion in neurobiology*, 25:156–163.
- Thalmeier, D., Uhlmann, M., Kappen, H. J., and Memmesheimer, R.-M. (2016). Learning universal computations with spikes. *PLoS computational biology*, 12(6):e1004895.
- Van Vreeswijk, C. and Sompolinsky, H. (1996). Chaos in neuronal networks with balanced excitatory and inhibitory activity. *Science*, 274(5293):1724–1726.

- Vogels, T. P. and Abbott, L. F. (2005). Signal propagation and logic gating in networks of integrate-and-fire neurons. *Journal of neuroscience*, 25(46):10786–10795.
- Vyas, S., Golub, M. D., Sussillo, D., and Shenoy, K. V. (2020). Computation through neural population dynamics. *Annual review of neuroscience*, 43:249–275.
- Wilson, H. R. and Cowan, J. D. (1972). Excitatory and inhibitory interactions in localized populations of model neurons. *Biophysical journal*, 12(1):1–24.
- Yamins, D. L. and DiCarlo, J. J. (2016). Using goal-driven deep learning models to understand sensory cortex. *Nature neuroscience*, 19(3):356–365.
- Zenke, F. and Vogels, T. P. (2021). The remarkable robustness of surrogate gradient learning for instilling complex function in spiking neural networks. *Neural computation*, 33(4):899–925.

## 6 Appendix

All code used to generate each figure in this article is available on GitHub at <https://github.com/wpodlaski/funcapprox-with-lowrank-EI-spikes>.

### 6.1 Network parameters in the single rank-1 population

For the single rank-1 population with 1-d input and 1-d output, neural parameters were chosen such that each neuron was tangent to a particular boundary curve, denoted  $y = -f_{cvx}(x)$ . Given a network of  $N$  neurons, boundaries were distributed uniformly along the curve in a particular input interval  $[x_A, x_B]$ , resulting in a tangent point  $(x_i, y_i)$  associated with each neuron. Then, each neuron’s voltage equation (Eq. (10)) at  $V_i = T_i$  was used to compute the parameters  $F_i$ ,  $E_i$ , and  $T_i$ . Given the redundancy of the three parameters, we arbitrarily set the encoding weight,  $E_i$ , to be 1 for each neuron. We thus have

$$E_i = 1, \tag{74}$$

$$F_i = -\frac{d}{dx} f_{cvx}(x_i), \tag{75}$$

$$T_i = F_i x_i + E_i y_i. \tag{76}$$

Then, the decoding weight  $D_i$  was chosen to achieve a particular jump size in the boundary at each value, and with sign constraint according to the population identity ( $D_i < 0$  for inhibition and  $D_i > 0$  for excitation).

To give a concrete example, let’s consider the boundary in Fig. 2b,c, with boundary function  $y = -x^2 - \frac{1}{2}$ . One neuron, say neuron  $i = 3$ , is tangent to the curve at the point  $(x_i = -0.5, y_i = -0.75)$ . This neuron’s parameters were set to

$$E_i = 1, \tag{77}$$

$$F_i = -\frac{d}{dx} f_{cvx}(x_i) = 2x_i = -1, \tag{78}$$

$$T_i = F_i x_i + E_i y_i = -0.25, \tag{79}$$

$$D_i = -0.35. \tag{80}$$

Note the negative threshold, with the interpretation that the neuron is spontaneously active due to an additional background current (see Eq. (1)). To constrain voltages to all be on the same scale, in practice we use a default threshold  $T_i^0 = 1$  for all neurons, and include a bias current  $b_i = T_i^0 - T_i$ . For the case of higher,  $M$ -dimensional input, as in Fig. 2e and Eq. (16), the procedure is analogous: a tangent point is designated for each neuron in  $M + 1$  dimensional space, and the feedforward weights simply become a  $M$ -dimensional vector with the gradient of the function  $-f_{cvx}(\mathbf{x}_i)$ .

## 6.2 Network parameters in the rank-2 EI network

Following a similar methodology as above for the single rank-1 population, here we consider fitting neural parameters of each population to a boundary in  $(x, y^E, y^I)$ -space. Specifically, we denote the inhibitory boundary as  $y^I = -f_{cvx}^I(x, y^E)$  and the excitatory boundary as  $y^E = -f_{cvx}^E(x, y^I)$ . Taking the inhibitory boundary as an example, neurons' tangent points were distributed in a 2d grid in intervals  $[x_A, x_B]$  and  $[y_A^E, y_B^E]$ , such that each neuron had an associated point  $(x_i, y_i^E, y_i^I)$ . Then, as before, encoders for self-connections,  $E^{II}$ , were set arbitrarily to 1 for all neurons. All parameters thus were set as

$$E_i^{II} = 1, \quad (81)$$

$$F_i^I = -\frac{\partial}{\partial x} f_{cvx}(x_i, y_i^E), \quad (82)$$

$$E_i^{IE} = -\frac{\partial}{\partial y^E} f_{cvx}(x_i, y_i^E), \quad (83)$$

$$T_i^I = F_i^I x_i + E^{IE} y_i^E + E_i^{II} y_i^I. \quad (84)$$

An analogous procedure was followed for the excitatory population. Once again, in principle decoders could be set arbitrarily following sign conventions ( $D_i^I < 0$ ,  $D_i^E > 0$ ). However, we found that in practice, decoders could be optimized to ensure the two populations take turns in spiking. We generally followed a heuristic that the effective direction that the decoders point towards should aim to counteract the leak dynamics at the boundary crossing point — in other words,  $D^I/D^E \approx y_*^I/y_*^E$ , where  $(y_*^E, y_*^I)$  is the crossing point of the two boundaries.

## 6.3 Function approximation in the rank-2 EI network

We consider the problem of approximating an arbitrary 1-d function  $f(x)$  within an interval  $[x_A, x_B]$  using the rank-2 EI spiking network, i.e., the general case of the example given in Figs. 5 and 12. To do so, we will take the following three steps: (i) find a piecewise-linear approximation to  $f(x)$ , denoted  $\tilde{f}(x)$ , such that  $\tilde{f}(x) \approx f(x)$  within  $[x_A, x_B]$ ; (ii) decompose  $\tilde{f}(x)$  into the difference of two convex functions, such that  $\tilde{f}(x) = f_{cvx}^E(x) - f_{cvx}^I(x)$ ; (iii) define the full boundary surfaces  $y^I = f_{cvx}^I(x, y^E)$  and  $y^E = f_{cvx}^E(x, y^I)$ , such that the solution for one of the populations yields  $\tilde{f}(x)$ .

**Piecewise-linear approximation:** We numerically find the second derivative of  $f(x)$ , denoted  $f''(x)$ . To heuristically find a good piecewise-linear approximation, we then find all of the minima and maxima of  $f''(x)$  within the interval. Given a desired number of piecewise-linear components, say  $P$ , we order the minima and maxima by absolute value and choose the top  $P + 1$  points, denoted  $x_p$ . We note that a similar procedure can be done using the maxima and minima of the function  $f(x)$  itself, resulting in a slightly different piecewise-linear approximation.

Using these points, we then approximate  $f(x)$  between each interval  $[x_p, x_{p+1}]$



as

$$\tilde{f}(x) = \frac{x - x_p}{x_{p+1}} f(x_p) + \frac{x_p + x_{p+1} - x}{x_{p+1}} f(x_{p+1}). \quad (85)$$

**Decomposition into the difference of two convex functions:** We now numerically find the second derivative of  $\tilde{f}(x)$ , denoted  $\tilde{f}''(x)$ . Due to  $\tilde{f}(x)$  being piecewise-linear,  $\tilde{f}''(x)$  will be zero everywhere except at the  $P + 1$  inflection points  $x_p$  defined above, and thus will appear “spiky”, with both positive and negative spikes. We then separate the second derivative by sign, as

$$(f_{cvx}^E)''(x) = \max[0, \tilde{f}''(x)] \quad (86)$$

$$(f_{cvx}^I)''(x) = \min[0, \tilde{f}''(x)]. \quad (87)$$

We then twice integrate these equations, using appropriate constants, in order to obtain the functions themselves  $f_{cvx}^E(x)$  and  $f_{cvx}^I(x)$ . It can then be verified that  $\tilde{f}(x) = f_{cvx}^E(x) - f_{cvx}^I(x)$ .

**Defining the full boundary surfaces in  $(x, y^E, y^I)$ -space:** For simplicity we assume that the  $I$  boundary is linear in  $y^E$ , and that the  $E$  boundary is linear in  $y^I$ , such that the two boundaries can be decomposed into the functional forms

$$y^I = -f_{cvx}^I(x) - 2y^E, \quad (88)$$

$$y^E = -f_{cvx}^E(x) - y^I. \quad (89)$$

Then, solving for  $y^E$ , we have

$$y^E = f_{cvx}^E(x) - f_{cvx}^I(x). \quad (90)$$

We include an example python notebook in the code repository that reproduces this process for randomly-generated 1d functions.

## 6.4 Synaptic dynamics

In Sections 2 and 3, we impose two very strict requirements on the synaptic dynamics: (i) we assume synaptic currents to be instantaneous, and (ii) we assume that inhibitory neurons always fire before excitatory neurons. The notion of instantaneous communication in a spiking network simulation with discrete time steps is tricky — technically speaking, even in models without synaptic delays, a delay equivalent to the simulation time step,  $dt$ , is implicit. Event-based simulators circumvent this problem by only integrating voltages up to the next spike. To keep the simplicity of a discrete-time simulation, we instead impose that only one neuron spikes per time step. For the single inhibitory population, the rationale is straightforward — when the first inhibitory neuron fires a spike, it will inhibit all other neurons in the network, and thereby prevent other neurons from spiking (provided  $dt$  is sufficiently small). For the EI network, an excitatory spike may instead drive other excitatory and inhibitory neurons above threshold. Here, we make the important assumption that inhibitory neurons will generally be driven above threshold faster than other excitatory neurons, and thereby are able to prevent additional excitatory spikes (see Discussion).

In Section 4, we eliminate these ad hoc rules and instead introduce finite synaptic dynamics in the form of exponential decay or square pulses. However, we generally keep the negative diagonal terms of the connectivity instantaneously fast, as they correspond to voltage resets. This corresponds to synaptic input of the form

$$\sum_{j=1}^N W_{ij} \alpha_j(t) - \mu s_i(t). \quad (91)$$